

DELFT UNIVERSITY OF TECHNOLOGY

---

# Literature Study

## Laser Propulsion System

---

Author:

Diogo Alexandre Martins Diogo Gomes (5447585)



# CONTENTS

<b>List of Figures</b>	<b>i</b>
<b>List of Tables</b>	<b>ii</b>
<b>Nomenclature</b>	<b>iv</b>
<b>1 Introduction</b>	<b>1</b>
<b>2 Laser and Optical System</b>	<b>4</b>
2.1 Laser System . . . . .	4
2.2 Reflective/Optical System . . . . .	7
<b>3 Receiver-Absorber Cavity</b>	<b>9</b>
3.1 Configuration and Efficiency . . . . .	9
3.2 Heat Balance . . . . .	11
3.3 Geometry . . . . .	11
3.4 Material . . . . .	16
3.5 Radiation . . . . .	17
3.5.1 Incoming Radiation Absorption . . . . .	17
3.5.2 Thermal Radiation Loss . . . . .	18
3.5.3 View Factors . . . . .	19
3.5.4 Gebhart Factors . . . . .	20
3.5.5 Geometry dependence . . . . .	21
3.6 Conduction . . . . .	22
3.7 Convection . . . . .	23
3.7.1 Inner Cavity Convection . . . . .	24
3.7.2 Single-Phase Propellant Convection . . . . .	26
3.7.3 Two-Phase Propellant Convection . . . . .	30
3.7.4 Outer wall convection . . . . .	31
3.8 Pressure Gradient . . . . .	32
3.9 Wall thickness . . . . .	34
3.10 RAC Tool . . . . .	35
<b>4 Nozzle</b>	<b>37</b>
4.1 Quantities and Efficiencies . . . . .	37
4.2 Geometry . . . . .	38
4.3 Ideal Rocket Theory . . . . .	39
4.4 Corretion Factors . . . . .	40
4.5 Nozzle Tool . . . . .	41

<b>5 Propellant System</b>	<b>43</b>
5.1 Storage and Feeding System . . . . .	43
5.2 Propellant . . . . .	44
<b>6 Experimental Research</b>	<b>46</b>
6.1 Laser Thermal Experiments . . . . .	46
6.2 Solar Thermal Experiments . . . . .	48
6.3 TU Delft Experiments . . . . .	50
<b>7 Conclusion</b>	<b>52</b>

# LIST OF FIGURES

1.1 Propulsion system thrust/weight ratio and specific impulse values [5]. . . . .	2
2.1 Schematic representation of the solar-pumped laser power station [13]. . . . .	5
2.2 Laser beam gaussian distribution and beam diameter . . . . .	5
2.3 Schematic representation of the solar-pumped laser power station [16]. . . . .	6
2.4 Spacecraft architecture overview - Inflatable Parabolic Reflector [6]. . . . .	8
3.1 Conical RAC (cross-sectional view) [31]. . . . .	10
3.2 Shoji J.'s candidate windowless cavity absorber configurations [36]. . . . .	12
3.3 The three studied geometry shapes of cavity receivers [33]. . . . .	12
3.4 Optical efficiency for the three cavity receivers at different receiver positions (mm) and absorptivity of; (a) 85% and (b) 75% [33]. . . . .	13
3.5 The illumination uniformity factor of the three cavity receivers at different receiver positions (mm) and absorptivity of; (a) 85% and (b) 75% [33]. . . . .	14
3.6 Four-parameter cavity receiver diagram and examples of geometries [37]. . . . .	14
3.7 Evolution of the simulated population of geometries during the stochastic optimisation process. For each $Q_{abs}$ , the performing geometries count is shown on top and the underperforming geometries count is located at the bottom of the bars [37]. . . . .	15
3.8 Three geometries obtained after the two stages optimisation. Vertical dotted lines indicate the beginning and end of the cone element [37]. . . . .	15
3.9 Incident flux patterns chosen for the study (a) collimated flux, (b) diffuse flux, and (c) focused incident flux. [48] . . . . .	18
3.10 Variations of $Q_c$ for a cylindrical cavity in different conditions [61]. . . . .	25
3.11 Convection heat loss for different geometries [53]. . . . .	26
3.12 The development of a two-phase flow in a vertical tube with a uniform wall heat flux (not to scale) [34] . . . . .	30
3.13 The boiling curve of water at 1 atm and various heat transfer regimes [68]	31
4.1 Nozzle Shape [4]. . . . .	39
4.2 Typical nozzle shapes [4]. . . . .	39
5.1 Ariane 5 Aestus stage [4]. . . . .	44
6.1 Eguchi's schematic of the experimental equipment [88] . . . . .	47
6.2 Mori's experimental setup [87] . . . . .	47
6.3 Shimizu M. et al. single crystal molybdenum solar thruster structure [90] .	48
6.4 Tucker S. et al. experiment configuration [91] . . . . .	49
6.5 Leenders H.'s test setup [31] . . . . .	50

# LIST OF TABLES

3.1	Possible RAC material choices and their characteristics [40] . . . . .	17
3.2	Radiative Heat Loss with unitary aperture ratio with varying temperature and emissivity for conical and cylindrical cavities . . . . .	21
3.3	Radiative Heat Loss with aperture ratio equal to 0.5 with varying temperature and emissivity for conical and cylindrical cavities . . . . .	22
3.4	Comparison of model and experimental results . . . . .	36

# NOMENCLATURE

## **Abbreviations**

*RAC* Receiver-absorber cavity

*TUD* Technische Universiteit Delft

## **Greek Symbols**

$\alpha$  Thermal expansion coefficient, Absorptivity

$\alpha_v$  Void fraction

$\epsilon$  Absolute roughness

$\eta$  Efficiency

$\Gamma$  Vandenkerckhove function

$\gamma$  Specific heat ratio

$\lambda$  Wavelength

$\mu$  Dynamic viscosity

$\phi$  Two-phase multiplier

$\rho$  Density

$\sigma$  Attenuation coefficient, Stefan-Boltzmann constant, Allowable stress

$\theta$  Divergence angle

$\theta_{mom}$  Momentum thickness

$\varepsilon$  Emissivity

## **Latin Symbols**

$\dot{m}$  Mass flow

$A$  Area

$a$  Aperture radius

$B_{ij}$  Gebhart factor

$C_d$  Discharge Coefficient

$c_p$  specific heat capacity

$D$  Diameter

$D_c$  Spiral diameter

$D_h$  Hydraulic diameter

$f_{DB}$  Darby-Weisbach factor

$F$  Thrust

$F_{ij}$  View factor

$G$  Flow rate

$g_0$  standard gravity

$Gr$  Grashof number

$Gz$  Graetz number

$h$  Height, Convective heat transfer coefficient

$I_{sp}$  Specific impulse

$j$  Safety factor

$K$  Beam profile constant

$k$  thermal conductivity

$L$  Length

$L_s$  Characteristic length

$M$  Molar mass

$m$  mass

$Nu$  Nusselt number

$P$  Power, Perimiter

$p$	Pressure	$conv$	Convection
$Pr$	Prandtl number	$cr$	Critical
$R$	Specific gas constant	$cyl$	Cylinder
$r$	Radius	$e$	Exit
$R_A$	Absolute gas constant	$e_t$	Themarl entrance
$Ra$	Rayleigh number	$eq$	Equivalent
$T$	Temperature	$f$	Final
$t$	Time, Thickness	$g$	Gaseous
$U, u$	Velocity	$i$	Initial, Inner
$u^*$	Friction velocity	$ins$	Insulation
$v$	Flight velocity	$l$	Liquid
<b>Subscripts</b>			
$abs$	Absorbed	$o$	Outer
$ac$	Acceleration	$p$	Propellant
$amb$	Ambient	$rad$	Radiation
$ap$	Aperture	$sp$	Single-phase
$c$	Chamber	$surf$	Surface
$cav$	Cavity	$t$	Throat
$con$	Cone	$tp$	Two-phase
$cond$	Conduction	$w$	Wall

# 1

## INTRODUCTION

Several spacecraft propulsion systems have been developed throughout the last decades [1]. For example, chemical propulsion has been consistently used by rocket engines [2] and electrical propulsion is commonly present in satellites for station-keeping purposes [3]. Other concepts, such as solar thermal propulsion and antimatter propulsion, have never flown in space or only the concept has been formulated. Each of these propulsion systems has its own advantages and disadvantages. Two of the most relevant quantities in propulsion are the specific impulse,  $I_{sp}$ , which is related to the amount of propellant mass needed for a certain thrust and dictates the amount of propellant required to be carried on board to perform a certain mission, according to the rocket equation; and thrust,  $F$ , which determines the acceleration that can be reached [4]. For instance, chemical propulsion has high thrust levels and low specific impulse which result in short burn times but high propellant mass needed, whereas electrical propulsion systems have high specific impulse but low thrust levels (fig. 1.1), leading to long burn times and, consequently, high gravity losses, despite their low mass requirements [4], as well as, high operational costs.

The current limitations of existing spacecraft propulsion systems, including high propellant mass requirements and long acceleration times, have resulted in payload restraints and high operational costs, making it challenging to explore deeper space missions. Consequently, there is a need for alternative propulsion systems that can address the limitations of existing spacecraft propulsion systems and enable more efficient and cost-effective deep-space exploration.

Laser thermal propulsion, as the name suggests, uses a laser as an energy source to accelerate a payload. It is a technology whose specific impulse and thrust levels have been proposed theoretically to be between the electrical and chemical propulsion values [5]. There are numerous ways to implement laser propulsion but this proposal is related to laser thermal propulsion via indirect heating, in which a laser is used to provide energy to the propellant by heating a heat exchanger. Researchers have also studied direct heating where the laser hits directly the propellant and absorbs its energy [6]. The laser can be on-board the spacecraft or located externally. The former requires the con-

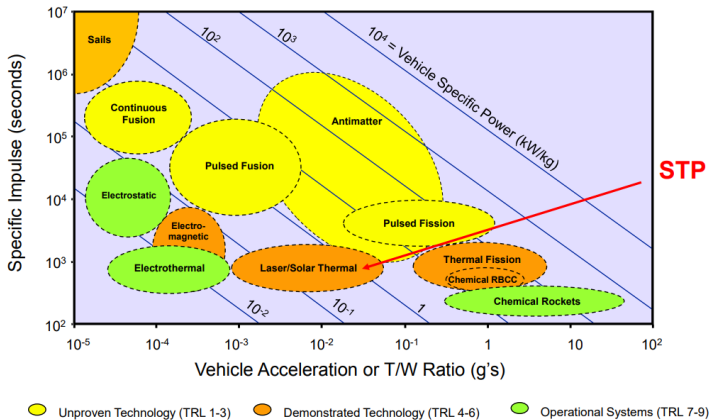


Figure 1.1: Propulsion system thrust/weight ratio and specific impulse values [5].

version of electrical (or solar) energy to laser energy while the latter suffers from beam spreading and needs a larger receptor. Using hydrogen as a propellant, a specific impulse as high as 800 seconds could be reached [7]. Recent research has suggested that a laser thermal propulsion system could be a solution to interplanetary travel [6]. Despite never having flown in space, it is a promising and creative technology whose further investigation could possibly lead to a new, reliable and efficient propulsion system alternative. The laser thermal propulsion system can be divided into the following distinctive components [6]:

- Laser system
- Optical/Reflective System
- Receiver/Absorber Cavity (RAC)
- Propellant and its tank, feed system and tubing
- Nozzle

Other additional elements may be present such as a thermal energy storage system, typically used in bi-modal propulsion systems [7]. However, the previous ones are crucial and the main focus of this literature study.

In addition, this technology is closely related to another interesting propulsion type: solar propulsion. In fact, solar propulsion uses a subsystem to focus the solar flux captured into a narrower beam which can be simulated as a laser [8]. Consequently, the outcomes of laser propulsion research can extensively be applied to solar propulsion which increases the utility and span of such analysis. Its mechanism is also similar to nuclear thermal propulsion, resistojets, and arcjets in the sense they use energy to heat propellant by nuclear reaction [9], electricity through a resistor [10], and electric discharge [11], respectively.

---

The aim of the literature study is to thoroughly investigate laser thermal propulsion by analyzing available literature, comprehending the key components, evaluating the current state-of-the-art, and identifying potential breakthroughs. Upon completion of the literature study, a thesis will be developed, taking into account all the information gathered.

Firstly, in chapter 2, an overview of the laser and reflective/optical system is done. The physics of laser as well as state-of-art options and performance for its subsystem are discussed. Additionally, the importance of the mirrors and lenses that redirect the laser is examined.

The RAC is the main object of study for this literature study and is the topic of chapter 3. After defining its configuration and relevant efficiencies, the geometries analysed in the literature and their performance is mentioned. Moreover, the heat transfer mechanisms and their dependencies are discussed. The tool developed in Matlab, which takes into account the knowledge gathered to predict the RAC's performance, is also presented.

In chapter 4, the theory behind the nozzle subsystem, ideal rocket theory, is briefly explained. Furthermore, correction factors to approximate the ideal to the real performance are presented. Next, in chapter 5, the propellant system is discussed. The storage and feeding system are stated but, more importantly, the propellant choices found in the literature are examined. From those, a few are selected to be appropriate for a potential experimental setting.

Experimental research is discussed in chapter 6. Due to the lack of a significant number of laser thermal experiments, relevant solar thermal experiments are also described. The main goal is to understand previous experiment setups and measurement techniques. Experiments performed in the faculty are also discussed.

Lastly, in the last chapter, conclusions are drawn from the information and data found in the literature.

# 2

## LASER AND OPTICAL SYSTEM

At the heart of any laser propulsion system is the laser itself, which generates the intense beam of light that is used to heat and accelerate the propellant. However, the laser is just one component of a complex system that includes mirrors, lenses, and other optical components that are used to shape and direct the laser beam. In this chapter, the laser and reflective/optical systems are explored, including a discussion of the key components and their roles in the propulsion process. Additionally, some of the current challenges and opportunities associated with these systems are examined.

### 2.1. LASER SYSTEM

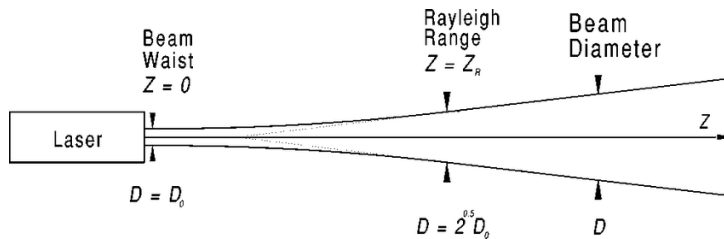
Needless to state that without a laser production system, there is no laser thermal propulsion. Thus, it is an undeniably fundamental component, whose characteristics are quite complex. Laser is actually an acronym for light amplification by stimulated emission of radiation which explains its functioning quite well. The gain medium is typically excited by an electrical current or another light source, which causes it to emit photons. These photons then bounce back and forth between the mirrors, passing through the gain medium multiple times and stimulating the emission of additional photons. This process amplifies the light, producing a highly collimated and coherent beam of light with a single wavelength or colour.

Due to their coherence, lasers appear to create a straight beam, however, laser beams eventually diverge. In the initial length called the Rayleigh distance, the beam is considered parallel [12]. Afterwards, the light waves start deviating according to the diverging angle  $\theta$ :

$$\theta = \frac{K\lambda}{D_e}, \quad (2.1)$$

where  $\lambda$  is the wavelength,  $D_e$  is the emission aperture's diameter and  $K$  is constant dependent on the beam's profile. The divergence of a laser beam is illustrated in fig. 2.1.

Regarding the beam profile, most lasers are gaussian i.e. their beam intensity follows a gaussian distribution (fig. 2.2). Although less common, there are also tophat laser



2

Figure 2.1: Schematic representation of the solar-pumped laser power station [13].

beams which have near-uniform intensities. Due to the nature of a gaussian distribution, it is difficult to pin down a precise definition for the beam diameter. Nevertheless, the most common definition is the one that limits the width to the area whose intensity is greater than  $1/e^2$  % or approximately 13.5% (Fig. 2.2).

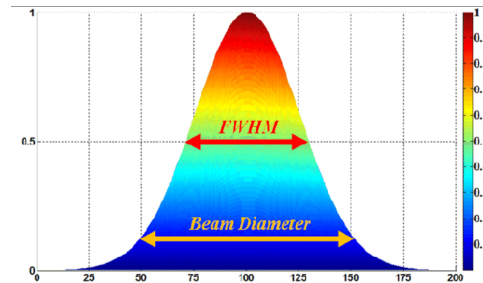


Figure 2.2: Laser beam gaussian distribution and beam diameter

The laser system efficiency is simply calculated by the ratio between the laser's beam incident energy on the propulsion system,  $P_{rec}$ , and the total electrical energy supplied to it,  $P_{in}$ :

$$\eta_{laser} = \frac{P_{rec}}{P_{in}}. \quad (2.2)$$

This definition differs from the famous wall plug efficiency (ratio between the laser's beam energy output and electrical energy supplied) but is necessary due to possible losses within the propagation medium. Despite its seeming simplicity, there are several factors that determine its value. For instance, it depends on the efficiency of the power supply, the efficiency of energy transfer to the particles and their excitation efficiency, and the ratio of particles that is effectively emitted. In general, depending on the laser, its efficiencies are not incredibly high. In 2016, IPG Photonics stated that their industrial fibre lasers with CW output power level from 1 to 10 kW surpassed 50% wall plug efficiency and that the lasers could easily be scaled up to tens of kW [14]. Unfortunately, the exact range efficiency values generally stated in literature are not always comparable as their efficiency definition is not consistent. For example, authors also typically use the slope efficiency which is the ratio between laser output energy and pump input energy [15], ignoring aspects such as the pump's efficiency and the energy spent in cooling

systems (which are usually required in high-powered lasers and critical regarding scalability).

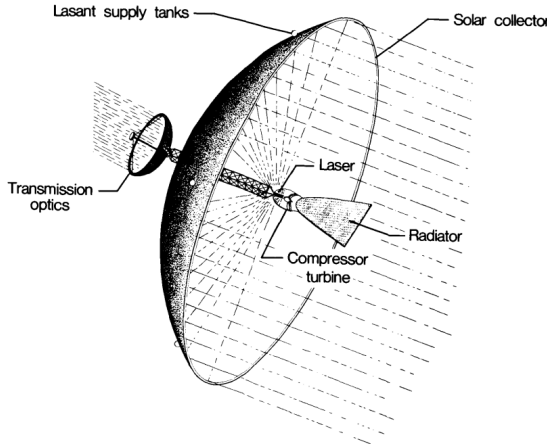


Figure 2.3: Schematic representation of the solar-pumped laser power station [16].

The location of the laser system is undeniably relevant. It can be located on earth, on a spacecraft or on another celestial body, for example, the moon. Laser-carrying space-craft with output power in the order of kW have been proposed to deal with, for instance, space debris removal [17]. Also, in 1987, De Young J. et al. published a paper regarding the cost analysis and design of a 1-Megawatt solar-pumped iodide laser (fig. 2.3) [16]. However, considering that the laser output needed is significantly high, the size, energy input and weight requirements of the system are a relevant concern for the last two options. The main disadvantage of an earth-based laser system is the presence of an atmosphere. In fact, the incident radiation energy will be reduced due to atmospheric absorption, particles can scatter the laser and limit the beam quality, and refraction of the laser can occur which increases the aiming difficulty. This subject is highly studied in the areas of climate change and remote sensing, for instance, where computational methods are used to predict these phenomena [18]. However, for instance, techniques such as adaptive optics can be applied to erase the beam distortions caused by Earth's atmosphere [19]. The laser's wavelength is ought to be chosen to fall within the transmission windows of the atmospheric absorption spectra to minimize losses and, thus, the contributions of absorption to the total attenuation coefficient are minimal and the effects of scattering dominate [20]. The laser attenuation is determined by the Beers-Lambert Law:

$$\frac{P(r)}{P(0)} = \exp(-\sigma r), \quad (2.3)$$

where  $\sigma$  is the attenuation coefficient, which depends on the visibility and the wavelength [21]. Higher wavelengths lead to lower attenuation.

In terms of attitude control of the laser, the planetary-based one can be pointed easily

with more accuracy. Still, there is less flexibility in terms of, for example, aiming periods and weather conditions. The spacecraft option requires additional systems to provide effective pointing accuracy which leads to higher mass and costs but does provide more flexibility.

To sum up, from the options, the earth-based laser system is the most feasible option. Nevertheless, the solar-pumped laser spacecraft is an interesting concept whose costs could be justified with several launches. The lunar option has too much downside, as of right now, for the only upside being the absence of a meaningful atmosphere. The laser system beam power efficiency can be expected to be at least 50% while the atmospheric attenuation can be minimized by choosing a proper wavelength [20].

## 2.2. REFLECTIVE/OPTICAL SYSTEM

The reflective/optical system typically includes a series of mirrors and lenses that receive, focus and shape the laser beam. The mirrors are typically made of high-quality, low-absorption and lightweight materials such as fused silica, which can withstand the high temperatures and pressures generated by the laser beam [22]. The efficiency of the reflective/optical system is determined by the ratio of the provided energy to the receiver/absorber cavity and the incident laser energy:

$$\eta_{opt} = \frac{P_{RAC, in}}{P_{rec}}. \quad (2.4)$$

This efficiency is mainly related to the elements' transmittance and the geometrical and spatial configuration.

Depending on the design, it is highly likely that this subsystem is the system's biggest component. Thus, rigid mirrors are not suitable due to their heavy weight. Inflatable space structures are an alternative which has been developed recently due to their compactness and lightweight [23]. Duplay E. et al. selected this technology for their off-axis mirror rapid transit to Mars mission (fig. 2.4) [6] and, also, Pino D. designed an inflatable solar concentrator for solar thermal propulsion [24]. By using appropriate material, such as dielectric silica coatings, it is possible to achieve mirror reflectivity values above 99% [25].

Due to the high laser energy, temperature limits are a concern regarding the components of this subsystem. Even though they have extremely low emissivity values, the laser energy density is incredibly high and, thus, should be calculated to ensure proper functioning. Consequently, there might be a need to increase the area of some elements, and, therefore, increase system mass to reduce their incident energy density to satisfy temperature requirements. Duplay et. al calculated this for their design and concluded that the temperature requirements were satisfied [6].

Furthermore, one important aspect of the reflective/optical system is controlling the shape and size of the laser beam. This can be achieved through the use of various types of mirrors and lenses, including parabolic mirrors and cylindrical lenses, which can shape the beam into a specific profile [26]. Another important consideration is the ability to direct the laser beam precisely onto the propellant, as even a slight misalignment can reduce the efficiency of the propulsion system and damage any other spacecraft component. Consequently, the reflective/optical system might require an active control system

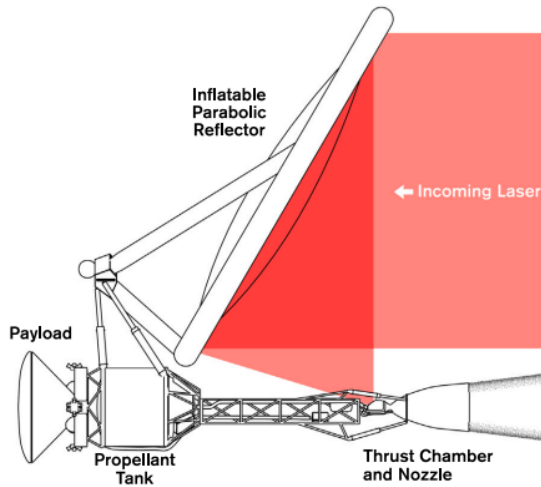


Figure 2.4: Spacecraft architecture overview - Inflatable Parabolic Reflector [6].

such as piezoelectric actuators to adjust and maintain proper mirror positioning [27] [28].

Concerning the lenses' transmittance, their values are usually high and range from 90% to 99%.

To sum up, the reflective/optical system requires extensive thermal, structural and optical analysis and considering the transmittance and emissivity values of currently available material, it seems realistic to assume an overall optical efficiency of at least 90%.

# 3

## RECEIVER-ABSORBER CAVITY

The receiver-absorber cavity (RAC) is an essential component of a beam-powered thermal propulsion system since it is where the heat from the beam is transferred to the working fluid, which is then expelled to provide thrust. Needless to say that the design of the RAC plays a crucial role in the overall performance of the system, as it affects the efficiency of the heat transfer process, pressure drop, cost and weight. This section explores possible RAC configurations, heat transfer mechanisms at play, various shapes, materials, pressure drops, mass and costs. Additionally, throughout, remarks about the choices and work performed previously at TUD are stated. By analyzing the existing literature, we aim to gain a better understanding of the critical factors that influence the performance of the RAC and to identify potential areas for further research and development.

### 3.1. CONFIGURATION AND EFFICIENCY

There are three possible RAC configurations that have also been mentioned by other previous students in solar thermal propulsion research: direct propulsion with direct absorption, direct propulsion with indirect absorption and indirect propulsion with indirect absorption [29] [30]. If the incoming radiation is used immediately to heat the propellant then it is direct propulsion; whereas if the energy is stored, for instance, in thermal storage, then it is considered indirect. Absorption can be direct if the radiation hits the propellant directly and indirect if it hits a medium that is in contact with the propellant. An example of direct propulsion with direct absorption is the design proposed by Duplay E. et al. [6] where there is a window in the propellant chamber that allows for the laser to hit the propellant there. Examples of direct propulsion with indirect absorption are the cavities developed at TU Delft by Leenders H. (fig. 3.1) [31] and Takken A. [8] that are heated up with the incoming radiation and the propellant is flowing in between its walls. Indirect propulsion with indirect absorption is out of the scope of this literature study.

The efficiency in the direct propulsion and absorption is related to the propellant's absorptivity [6]. However, hydrogen, the preferable propellant due to its low molar mass,

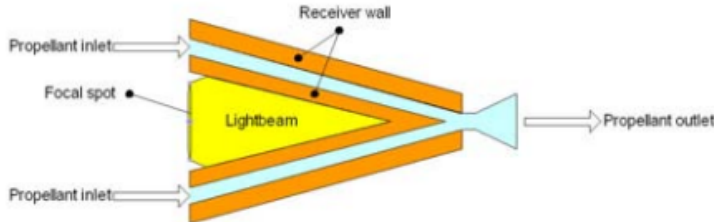


Figure 3.1: Conical RAC (cross-sectional view) [31].

3

has an inherent low absorption which presents itself as an obstacle. It is possible to seed the propellant with, for example, carbon particles that absorb the radiation and then heat the neighbouring hydrogen particles [32]. Although this can effectively fix the absorption problem, the carbon particles are also propelled and, therefore, increase the average propellant molar mass which defeats the purpose of hydrogen to some degree.

In the case of direct propulsion and indirect absorption, the efficiency can be divided into two crucial and somewhat independent efficiencies: absorption efficiency by the cavity material and heat transfer efficiency to the fluid. The first one is highly dependent on the incoming laser shape, cavity geometry and surface emissivity and values of 90% have been reached in literature [33]. In this case, the efficiency is calculated by:

$$\eta_{abs} = 1 - \frac{Q_{radloss} + Q_{convloss} + Q_{condloss}}{P_{RAC,in}}, \quad (3.1)$$

where  $Q_{radloss}$  is the radiation loss,  $Q_{convloss}$  is the convective heat lost to heat the medium, and  $Q_{condloss}$  is the heat lost via conduction. Radiation and convection loss by the RAC's outer surface can be greatly minimized by external insulation. Additionally, the conduction loss can be relatively small in a material with high thermal conductivity and a RAC with a low mass geometry. Thus, in that situation, the main optimization focus is the cavity's efficiency:

$$\eta_{cav} = 1 - \frac{Q_{radloss} + Q_{convloss}}{P_{RAC,in}}, \quad (3.2)$$

where the radiation and convection losses are only related to the cavity's inner surface.

The second efficiency is dependent on, for example, the propellant, its mass flow, contact surface area and tubing layout. Lienhard J. et al [34] state that this second efficiency, namely heat exchanger efficiency, is calculated by:

$$\eta_{hx} = 1 - \exp\left(-\frac{hPL}{mc_p}\right), \quad (3.3)$$

where  $h$  is the convective heat transfer coefficient,  $P$  and  $L$  are the cross-sectional perimeter and area of the duct, respectively, and  $c_p$  is the specific heat capacity of the propellant [34]. This formula does not take into account the energy transmitted to the propellant

via radiation which is present in significant temperature differences. Overall RAC efficiencies of 85% are attainable [33].

## 3.2. HEAT BALANCE

Thermal equilibrium is the state in which there is no net flow of heat between the system and its surroundings [35]. In other words, the rate of heat flow into the system is equal to the rate of heat flow out of the system:

$$Q_{in} = Q_{out} \Leftrightarrow \Delta Q_{syst} = 0. \quad (3.4)$$

The equilibrium temperature of a system depends on a variety of factors, including its size, composition, and the temperature of its surroundings. For example, if you place a cold object in a warm room, the object will begin to absorb heat from the surrounding air until it reaches thermal equilibrium with its environment. The equilibrium temperature of the object will depend on its size and composition, as well as the temperature of the surrounding air.

Considering that the laser is not turned on, the RAC is at a certain temperature  $T_0$ . As soon as the laser is turned on, the net flow of heat is no longer zero and the temperature evolves towards the equilibrium temperature  $T_{eq}$ . This transient analysis is described by the following equation [34]:

$$\frac{dQ_{syst}}{dt} = mc_p \frac{dT}{dt}, \quad (3.5)$$

where  $m$  is the RAC's mass, and  $c_p$  is the specific heat capacity of the material. The main result from equation (3.5) is that the temperature increase rate is dependent on the system's mass, and specific heat capacity of the material. For an equal amount of energy, greater  $m$  and greater  $c$  imply a lower increase rate in temperature. Thus, it is advantageous to optimize for lower mass and choose a material with low  $c$  if fast start-up times are a concern.

Several factors, such as geometry and tubing layout, determine the final temperature of the RAC and will be discussed in the following sections.

## 3.3. GEOMETRY

As mentioned previously, the RAC's efficiency is dependent on its efficiency to absorb the incoming radiation and as well to retain its inner emitted radiation, and, thus, its geometry plays an undeniable part [36] [33] [37]. Several shapes to satisfy this need have been proposed and analyzed to some degree.

Firstly, the RAC can be designed with or without a cavity. The latter option, despite its advantage in manufacturing as a result of its simplicity, is not appropriate due to its high reflective losses (the beam only hits the surface once, limiting absorption and there is no re-absorption of emitted radiation) and its high-temperature gradients (if the beam is focused on a too-small area, then it might heat up and melt). On the other hand, a cavity allows for the radiation to reflect inside it which results in an overall higher absorption of the incoming radiation, and more uniform temperature distribution as the energy is

spread out. Furthermore, the inner wall radiation is absorbed to some degree by itself which reduces the RAC's radiation losses [38].

3

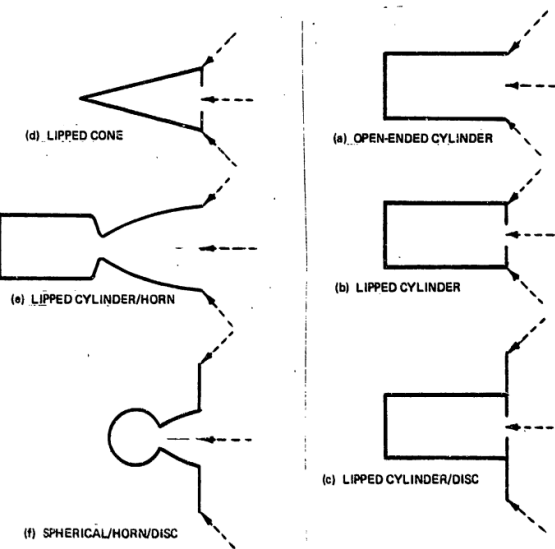


Figure 3.2: Shoji J.'s candidate windowless cavity absorber configurations [36].

In 1985, Shoji J. presented and investigated six different cavity shapes (Fig. 3.2) [36]. The method to evaluate the cavity absorber efficiency took into account incoming radiation, absorbed radiation, and lost radiation through the opening and outer walls. However, Shoji does not properly explain how he reached the final formulas which depend on, for example, view factors, areas and emissivities. From a personal perspective, the equations do not seem appropriate or accurate in any way as, for instance, reflections do not appear to be fully taken into account (Gebhart factors should probably make an appearance). Additionally, Takken, in his literature study, mentions that by performing a small sensitivity analysis on the equations, it was found that the outputted values largely made no sense or were too influential [30]. Also, the radiation is not considered to be focused into the cavity which is not ideal nor necessary with current technology. Therefore, the results from this research should not be considered to great extent. Nevertheless, Shoji concludes that a spherical/horn/disc shape and an open-ended cylinder are the most promising.

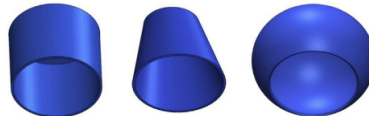


Figure 3.3: The three studied geometry shapes of cavity receivers [33].

Daabo A. et al. studied the effect of receiver geometry for parabolic solar applications

in terms of optical efficiency as well as flux distribution [33]. Three distinct geometries were studied: conical, cylindrical and spherical; and they had equal aperture diameter and inner surface area (fig. 3.3). Furthermore, several focal distances were used. The optical efficiency results are presented in fig. 3.4. The conical shape clearly presented the highest optical efficiency in all cases amongst the three candidates with the cylindrical showing better results for  $\epsilon = 0.85$  than the spherical, but for  $\epsilon = 0.75$  this relation switches. Also, the efficiency changes with the focal distance.

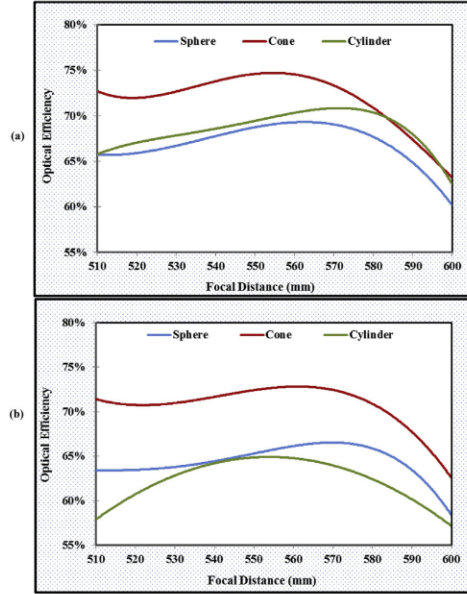


Figure 3.4: Optical efficiency for the three cavity receivers at different receiver positions (mm) and absorptivity of; (a) 85% and (b) 75% [33].

In order to calculate the energy uniformity, Daabo A. et al. used the following formula for the uniformity factor:

$$UF = \left( 1 - \frac{\text{Maximum irradiance} - \text{Average irradiance}}{\text{Maximum irradiance}} \right) \times 100\%, \quad (3.6)$$

where the average irradiance is the incoming energy divided by the inner surface area and the maximum flux was determined by the highest fluxed areas inside the receivers. The results are presented in fig. 3.5. Again, the conical shape stands out between the three as the one with the best energy distribution, and the cylindrical and spherical with close results dependent on the surface's absorptivity. In addition, the uniformity factor tends to be higher in the  $\epsilon = 0.75$  case since each section absorbs less and the reflected rays contain more energy which evens out the distribution.

From this study, it is clear that the conical cavity performs best in terms of optical efficiency as well as energy distribution. However, this conclusion can not be taken as a basis for a final choice since it is a study done for a specific case. In fact, the results show

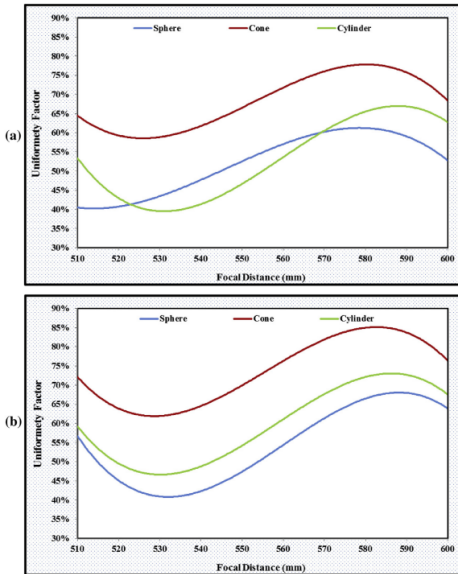


Figure 3.5: The illumination uniformity factor of the three cavity receivers at different receiver positions (mm) and absorptivity of; (a) 85% and (b) 75% [33].

that there are several variables that change the efficiency of the system and enhance the importance of performing tests for one's scenario. Furthermore, losses such as radiation are not taken into account and the beam is not fully focused on the aperture. Nevertheless, it is a good reference for why conical shapes might be the best option, and, thus, worth investigating.

Another paper by Asselineau C. et al. performed geometrical shape optimization of a cavity receiver using radiative as well as hydrodynamic models [37]. The shape of the cavity was influenced by four parameters which can result in various geometries. as shown in fig. 3.6.

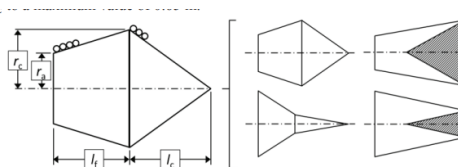


Figure 3.6: Four-parameter cavity receiver diagram and examples of geometries [37].

The optimization process was divided into two stages to decrease computational effort. The first stage focused on the radiative model where the amount of radiative power absorbed subtracted by thermal emission is maximised. In the second stage, a detailed heat transfer simulation is performed on the candidates selected from the previous stage. In this simulation, the hydrodynamic one-dimensional tube model is added

to the radiative modelling as well as the necessary components to relate them. To decrease the computational effort even further, a statistical model based on confidence intervals was implemented to eliminate the worst performers rapidly (fig. 3.7).

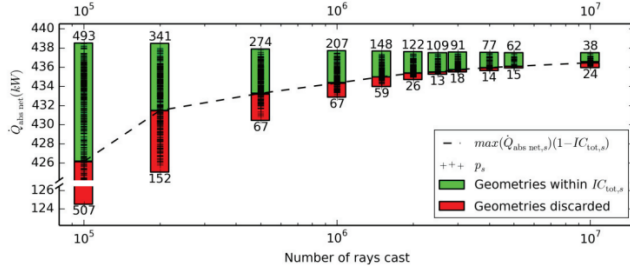


Figure 3.7: Evolution of the simulated population of geometries during the stochastic optimisation process. For each  $\dot{Q}_{abs}$ , the performing geometries count is shown on top and the underperforming geometries count is located at the bottom of the bars [37].

In fig. 3.8, three geometries of the final group are presented: case 03 is the best performer, case 29 is an intermediate performer, and case 13 is the worst amongst the 38. The final 38 best-performing geometries are undeniably diverse, as can be seen, and their efficiencies range between 82% and 87%. The efficiency is defined as the ratio between the fluid's absorbed heat and total incoming radiation. It also shows how different shapes that have similar efficiencies present disparate energy distribution and temperature profiles.

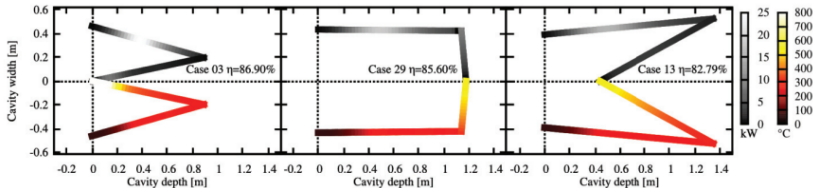


Figure 3.8: Three geometries obtained after the two stages optimisation. Vertical dotted lines indicate the beginning and end of the cone element [37].

Regarding work done by TUD students, Leenders H. chose the conical shape over the cylindrical, even though it entails fewer reflection losses, due to better distribution of incoming radiation on the walls [31]. It is important to mention that Leenders' cavities are not lipped which influences the reflection losses and radiation distribution. The trade-off does not appear extensive as there is no investigation on how the incoming radiation distribution influences performance. For example, it likely affects the time it needs to reach the equilibrium temperature but does not necessarily result in higher temperatures. Additionally, the reflection loss calculations are not provided.

In 2015, Preijde J. analyzed conical, cylindrical and spherical shapes throughout their thesis and preferred the cylindrical cavity after performing a trade-off which took into account: specific impulse, system-specific impulse, thrust, wet system mass fraction, system volume, and system complexity [39]. To calculate the radiation absorbed by the

RAC, Preijde J. works with view factors which might provide a fair estimate but are not correct, as it will be explained in section 3.5.3. Thus, his preference for a cylindrical cavity is not fully substantiated.

**3**

Das K. only analyzes rectangular and trapezoidal RAC shapes and chooses a rectangular shape after a wide-ranging trade-off [29]. The efficiency of the RAC is assumed directly related to the surface area available for heating which is an unjustified assumption. For instance, a high surface area needs more energy to heat up the RAC. Furthermore, Takken A. chooses the lidded cylindrical cavity due to its more than reasonable performance and easiness to manufacture and argues that the slight increase in mass compared to a conical shape is compensated by an increase in tubing length which increases heat efficiency [8]. Also, Takken A. incorporated a significant spike inside the cavity to try to improve the beam's energy distribution into the inner walls. This was decided without any significant analysis to support it. Despite the possible positive outcome in energy distribution, the downsides seem to outweigh it: the system mass is increased which leads to higher heating times and higher losses in conduction, and the inner wall surface is increased which leads to higher radiation losses.

Considering the information available in the literature and cavity simplicity, the conical and cylindrical cavities appear to be the best candidates for further analysis. In addition, a cylinder with a conical bottom geometry, similar to case 29 in fig. 3.8, is also worth looking into: the conical bottom might lead to a higher number of reflections in the wall, improving energy distribution and beam absorption, and lower pressure losses due to not-so-significant bending.

### 3.4. MATERIAL

The material choice undeniably affects the RAC's efficiency and, thus, the performance of the propulsion system. Regarding the inner wall, its selection is fundamental as it is the target of the incoming radiation. Consequently, some fundamental characteristics are desired: high melting point  $T_{melt}$  allows for a higher RAC temperature, which results in higher fluid temperatures, without compromising any structure and thermal integrity; high thermal conductivity  $k$  facilitates the transfer of heat from the inner wall to the working fluid and increases temperature uniformity; low thermal expansion coefficient  $\alpha$  to withstand the high temperatures encountered; low density  $\rho$  to have a lower mass. Furthermore, specific heat capacity  $c_p$  determines the rate at which the RAC heats up, it has no direct influence on overall performance, but a low value might be desirable. Additionally, from a low-budget project point of view, cost and manufacturability are also relevant. As far as emissivity goes, it will not be criteria as a coating can be applied and the value changes depending on wavelength.

From the literature, there are several candidates to satisfy the RAC's needs and the most relevant are listed in table 3.1. Kennedy F. and Palmer P. evaluated, for instance, graphite whose primary drawback is the potential for reactivity with propellants of interest at high temperatures [43]. AFRL's ISUS program [44] as well as Shoji [45] chose a rhenium-coated graphite cavity but the coating adds complexity due to differential thermal expansion and cracking [43]. Kennedy F. and Palmer P.'s final choice is a Boron Carbide ( $B_4C$ ) wall with a Boron Nitride (BN) protection [43]. However, their choice was based on the desire to have a receiver with high energy density and, thus, high specific

Table 3.1: Possible RAC material choices and their characteristics [40]

Material	$T_{Melt}$ (°C)	$k$ (W/m-K)	$c_p$ (J/Kg-K)	$\rho$ (g/cm³)	$\alpha$ (μm/m-K)	Cost [41] (€/kg)
Copper	1084	342	385	8.79	16	5.90
Molybdenum	2620	105	272	10.2	5	16
Rhenium	3186	45.7	140	21.4	6.7	1635
SiC	2730	120	670	3.16	2.77	-
Tungsten	3400	115	132	19.2	4.5	25.52
Graphite [42]	3652	*	706.9	1.9-2.3	-	-

\*Carbon conductivity varies widely with the exact form, and is anisotropic. Values range from 1960 (graphite, in a plane, 300 K) to 2.3 (amorphous) [42].

heat which is not advantageous for the system's start. Due to their low specific heat capacity, high thermal conductivity, and high melting point, molybdenum and tungsten are commonly suggested by researchers [39] [29] [30] [36] [7]. Rhenium is also suggested but usually falls behind the previous two options due to its relatively lower thermal conductivity. More recently, Japanese researchers have used Carbon-fiber entangled porous material to perform experimental work [46] [47]. Leenders H. built a copper RAC at the faculty since the aimed temperatures were lower than copper's melting point and the material provides high thermal conductivity and low specific heat capacity for low cost [31]. Also, Takken A. used copper mainly due to budget limitations [8].

## 3.5. RADIATION

### 3.5.1. INCOMING RADIATION ABSORPTION

The first process to be evaluated is the absorption by the RAC of the incoming radiation. The radiation hits the walls and absorbs a percentage of the total power which depends on the material's optical properties or the coating (emissivity or absorptivity). Furthermore, the reflected radiation might still hit the wall again, depending on the geometry, which increases the overall absorption. Thus, the absorbed power  $P_{abs}$  is:

$$P_{abs} = \eta_{abs} P_{RAC,in}, \quad (3.7)$$

where  $P_{RAC,in}$  is the incoming radiation power and  $\eta_{abs}$  is the efficiency of the transfer which depends on the emissivity  $\epsilon$  or the absorptivity  $\alpha$  of the surface, the surface's diffuse ratio value, the geometry of the RAC and the incoming radiation. In the simplistic case, where the radiation hits the surface and does not absorb any reflection,  $\eta_{abs}$  would just be  $\epsilon$  or  $\alpha$  depending on the wavelength. Consequently,  $\eta_{abs}$  cannot be lower than these values as the radiation absorption can only be increased from the simplistic scenario.

Radiation reflection can be either specular or diffuse. In smooth surfaces such as mirrors, the former occurs and radiation reflects at the same angle of incidence; whereas in rougher surfaces, the latter phenomenon occurs and the rays scatter in different directions [38]. Diffuse reflection increases the complexity of the incoming radiation absorption analysis [48]. Larrouturou F. et. al studied the effect of directional dependency

of wall reflectivity in a cubical solar cavity in both specular and fully diffuse scenarios [48]. The cavity aperture was the whole side and three scenarios were studied (fig. 3.9). A Monte-Carlo ray tracing method was implemented.

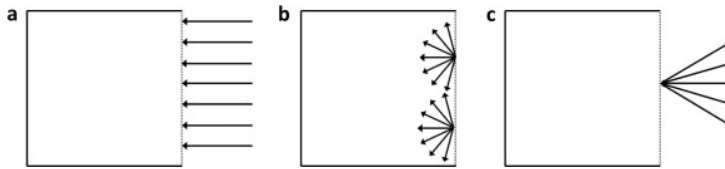


Figure 3.9: Incident flux patterns chosen for the study (a) collimated flux, (b) diffuse flux, and (c) focused incident flux. [48]

In the collimated flux case, the specular surface's absorption is entirely dependent on the bottom surface's emissivity. On the other hand, the diffuse case presents higher absorption rates for any emissivity value. This is expected since, in the diffuse case, the only absorption of the specular case always occurs and additional reflections are absorbed. The second scenario presents higher absorption rates than the first but an increase in the wall's diffuse ratio leads to lower absorption. The final case shows that there is a tendency for higher radiation absorption with the opening angle. This phenomenon is somewhat predictable since an increase in the opening angle should lead to an increase in the number of reflections in the side walls. Furthermore, it seems that an increase in an opening angle above 50° does not result in significant improvements. Also, the average number of reflections reaches a maximum in the middle diffuse ratio values. Consequently, this study shows that the surface's emissivity, incoming radiation geometrical conditions and surface's diffuse ratio play a role in the absorption.

### 3.5.2. THERMAL RADIATION LOSS

The RAC experiences thermal radiation losses which can be significant due to its high temperature. The two main sources of energy loss via thermal radiation are the cavity's inner wall and the RAC's exterior wall.

The rate of heat transfer by emitted radiation  $Q_r$  by a surface is determined by the Stefan-Boltzmann law of radiation [34]:

$$Q_r = \sigma \varepsilon A_{surf} (T_{surf}^4 - T_{amb}^4), \quad (3.8)$$

where  $\sigma$  is the Stefan-Boltzmann constant,  $\varepsilon$  is the surface's emissivity,  $A_{surf}$  is the surface's area, and  $T_{surf}$  and  $T_{amb}$  are the surface's and surrounding's temperature, respectively. Furthermore, the emitted radiation from surface 1 that hits surface 2  $Q_{12}$  requires the addition of the view factor term  $F_{12}$ :

$$Q_{12} = F_{12} \sigma \varepsilon A_{surf} (T_{surf}^4 - T_{amb}^4). \quad (3.9)$$

The view factor depends on the orientation of the surfaces and their geometry, which will be explained further in 3.5.3.

Regarding the inner wall's radiation loss, this will be highly determined by its geometry, more specifically, its view factors, and its surface's emissivity. Due to it being a cavity,

some of the emitted radiation will be absorbed by another surface. By minimizing the radiation able to escape, the RAC's efficiency can be improved.

The exterior wall does not have the same ability to reabsorb by itself some of the emitted radiation and the main factor for its loss will be its temperature, area and emissivity. Thus, it is interesting to analyze how the temperature could be lowered in the outer wall or how it could be insulated. For instance, MLI insulation, which is highly used in the space industry, could be applied to reduce drastically the radiation losses [49]. Additionally, Leenders H.[31] used Saffil M-Fil insulation whose properties can be found in its data sheet [50]. In his thermal model, Leenders H. showed that by adding the insulation the RAC temperature increased by 200 K to 300 K [31].

### 3.5.3. VIEW FACTORS

View factors are mathematical quantities used to determine the fraction of emitted radiation by a surface that is directly impinging on another surface [35]. More specifically, view factors are a measure of the geometric relationship between surfaces, taking into account the angle of incidence of the radiation and the shape of the surfaces [38]. Additionally, view factors are not suitable for the analysis of laser beams, as they are based on the assumption of diffuse radiation coming from all directions [35].

It's worth noting that the calculation of view factors can be quite complex, it's not always possible to obtain the view factor algebraically, especially for complex geometries [51]. In these cases, numerical methods must be used. Nevertheless, there are three important and trivial relations that are always respected [38]:

$$\sum_j F_{i,j} = 1, \quad (3.10)$$

$$A_1 F_{12} = A_2 F_{21}. \quad (3.11)$$

$$F_{1(23)} = F_{12} + F_{13} \quad (3.12)$$

The first one (eq. (3.10)) states that the sum of all view factors from one surface to the others is one since all the emitted radiation is directed to some surface (energy conservation). The following relationship (eq. (3.11)) is related to the reciprocity of the heat transfer between two surfaces. This relationship is useful in simplifying the calculation of view factors, as it allows for the determination of a single view factor when the other is known. This can be especially useful in complex systems where the direct calculation of all view factors may be difficult. The last one (eq. (3.12)) describes that the view factors can be added due to their intersection being null. This allows for some simplifications in calculations, for instance, that involve outer rings [51].

#### Cylinder

Considering a cylinder with an aperture on one of its sides, only the lateral and bottom surfaces are directly emitting radiation to the aperture. However, radiation from the aperture's outer ring can also escape to the exterior due to inner reflections and that can be calculated via Gebhart factors which will be explained in section 3.5.4.

Let surface 1 be the bottom surface, surface 2 the lateral side, surface 3 the aperture's outer ring, and surface 4 the aperture itself. Based on [51], some of the view factors are:

$$x = 1 + \frac{1 + R_2^2}{R_1^2}, \quad R_1 = \frac{r}{h}, \quad R_2 = \frac{a}{h}, \quad (3.13a)$$

$$F_{14} = \frac{1}{2} \left( x - \sqrt{x^2 - 4 \left( \frac{a}{r} \right)^2} \right), \quad F_{13} = \frac{1}{2} \left( 2 + \frac{1}{R_1^2} - \sqrt{\frac{2}{R_1^2} + \frac{1}{R_1^4}} \right) - F_{14} \quad (3.13b)$$

$$F_{12} = 1 - F_{13} - F_{14}, \quad F_{21} = \frac{R_1}{2} F_{12}, \quad F_{22} = 1 - 2F_{21}, \quad (3.13c)$$

$$F_{24} = \frac{1}{2rh} (a^2 - r^2 F_{14}), \quad (3.13d)$$

where  $r$  is the cylinder radius,  $a$  is the aperture's radius and  $h$  is its height. The view factors are undeniably complex and the directly lost emitted radiation is calculated with  $F_{14}$  and  $F_{24}$  which do not present trivial trends. Nevertheless, it is expected that the decrease of  $a$ , and the increase of  $r$  and  $h$  usually lead to lower radiation losses. Not all of the view factors are presented but one can effortlessly calculate the remaining using view factor algebra (equations (3.10), (3.11) and (3.12)).

### Cone

Considering a cone with an aperture in its base, only the lateral side directly emits radiation towards the aperture. Let surface 1 be the cone's lateral side, surface 2 the aperture's outer ring and surface 3 the aperture itself and, from [51], the view factors are:

$$F_{11} = 1 - \frac{1}{\sqrt{1 + L^2}}, \quad F_{12} = \frac{1 - R^2}{\sqrt{1 + L^2}}, \quad L = \frac{h}{r}, \quad R = \frac{a}{r}, \quad (3.14a)$$

$$F_{13} = \frac{R^2}{\sqrt{1 + L^2}}, \quad F_{21} = 1, \quad F_{31} = 1, \quad (3.14b)$$

where  $h$  is the height of the cone,  $r$  is the base radius, and  $a$  the aperture radius. Thus, the view factors depend on two ratios: the aperture ratio, and the base and height ratio. The view factor related to direct radiation loss is  $F_{13}$  and it can be lowered by increasing the height and base radius ratio and by decreasing the aperture ratio. However, lowering  $F_{13}$  does not necessarily mean lower radiation loss since the area of surface 1 could have been increased in the process, which can result in higher radiation loss. Unlike the cylinder's case, the view factors are irrefutably less complex.

#### 3.5.4. GEBHART FACTORS

The view factors, as mentioned, only account for the fraction of a surface's emitted radiation that arrives at other surfaces and, unless that surface is a black body, it will not absorb all the radiation and some of it will be reflected somewhere [51]. Thus, Gebhart B. developed the Gebhart factors which effectively calculate the fraction of radiation that is absorbed: it considers all the reflections [38]. Even though the calculation of these

Gebhart factors requires the previous calculation of the view factors, it still requires less computational power than using Monte-Carlo ray tracing [52]. Similarly to the view factors, from [38], Gebhart factors obey to some laws:

$$\sum_j B_{ij} = 1, \quad (3.15a)$$

$$\varepsilon_i A_i B_{ij} = \varepsilon_j A_j B_{ji}. \quad (3.15b)$$

The first equation is related to energy conservation and the second states that the rate of heat transfer between two surfaces has equal magnitude (reciprocity).

The Gebhart factors for an n-surface enclosure can be calculated by the following equation [38]:

$$B_{ij} = F_{ij}\varepsilon_j + \sum_k^n (1 - \varepsilon_k)F_{ik}B_{kj}. \quad (3.16)$$

From the equation (3.16), it is fairly easy to understand that it is not as straightforward as the view factors since each Gebhart factor depends on the values of others. Consequently, calculating the Gebhart factors is essentially solving a linear system. However, only  $n(n-1)/2$  independent factors, in an n surface system, need to be calculated directly as the Gebhart factor algebra can easily determine the rest [38].

### 3.5.5. GEOMETRY DEPENDENCE

As shown previously, the geometry highly determines the view factors and, thus, it is expected that the radiation loss is dependent on it. However, Jilte R. et al. calculated the radiative heat loss for several cavity geometries for a fixed diameter and unitary emissivity and the values practically do not change between geometries in both case studies (the first one with equal heat transfer area for convection and the second equal length and diameter ratio) [53]. A Matlab model was built for cylindrical and conical shapes to calculate their respective radiative heat loss and, consequently, verify the previously mentioned trend. In the model, the aperture ratio was changed as well as the emissivity and the results are in tables 3.2 and 3.3.

Table 3.2: Radiative Heat Loss with unitary aperture ratio with varying temperature and emissivity for conical and cylindrical cavities

$T_w$ (K)	523	723	923
$Q_{cyl}$ ( $\varepsilon = 1$ ) (W)	750.78	2960.0	7998.5
$Q_{con}$ ( $\varepsilon = 1$ ) (W)	750.78	2960.0	7998.5
$Q_{cyl}$ ( $\varepsilon = 0.9$ ) (W)	739.34	2914.9	7876.6
$Q_{con}$ ( $\varepsilon = 0.9$ ) (W)	725.29	2859.6	7727.0
$Q_{cyl}$ ( $\varepsilon = 0.8$ ) (W)	725.47	2860.2	7728.8
$Q_{con}$ ( $\varepsilon = 0.8$ ) (W)	695.77	2743.2	7412.5

Firstly, the results from Jilte R. et al. are confirmed: the radiation loss is equal for the two if the emissivity is unitary [53]. However, from both tables, it is clear that this trend

Table 3.3: Radiative Heat Loss with aperture ratio equal to 0.5 with varying temperature and emissivity for conical and cylindrical cavities

$T_w$ (K)	523	723	923
$Q_{cyl}$ ( $\epsilon = 1$ ) (W)	187.69	740.0	1999.6
$Q_{con}$ ( $\epsilon = 1$ ) (W)	187.69	740.0	1999.6
$Q_{cyl}$ ( $\epsilon = 0.9$ ) (W)	186.95	737.1	1991.7
$Q_{con}$ ( $\epsilon = 0.9$ ) (W)	186.10	733.7	1982.6
$Q_{cyl}$ ( $\epsilon = 0.8$ ) (W)	186.04	733.5	1982.0
$Q_{con}$ ( $\epsilon = 0.8$ ) (W)	184.22	726.3	1962.6

3

does not maintain when the emissivity is not unitary. Lower emissivity leads to lower radiative losses, as expected, and the conical shape presents lower values than the cylindrical when in the same aperture ratio and emissivity value. Nevertheless, the aperture ratio is undeniably the most important aspect. Comparing the values from tables 3.2 and 3.3, the change to an aperture ratio of 0.5 results in an approximate 75% radiative heat loss reduction. Furthermore, emissivity's influence in reducing the loss is diminished.

### 3.6. CONDUCTION

Conduction is the process of transferring heat through a solid material by means of molecular interactions. The heat is moved as warmer molecules come into contact and mix with or excite colder ones, resulting in the diffusion of heat within the material [34]. This is achieved without any net motion of the material as a whole. In this case, heat is transferred from the inner wall of the cavity to the outer areas in order to transfer heat to the fluid through direct contact. The wall must be able to efficiently transfer heat to the fluid, while also maintaining its structural integrity and avoiding thermal stress. The rate of heat transfer is dependent on the thermal conductivity  $k$  of the wall material and the temperature gradient between the wall and the fluid. From [34], the general equation for thermal conduction for the one-dimensional plane is:

$$Q_{conduction} = k \frac{dT}{dx}. \quad (3.17)$$

Concerning a cylindrical shell, Zandbergen [4] provides a steady-state unidirectional conduction formula:

$$Q_{conduction} = \frac{2\pi k L}{\ln\left(\frac{r_o}{r_i}\right)} (T_i - T_o), \quad (3.18)$$

where  $L$  is the cylinder's length,  $r$  the radius and the subscripts  $i$  and  $o$  the inner and outer surface, respectively.

Heat transfer in a cone is a more complex situation due to its varying radius and there are no theoretical solutions. Ray S. et al. investigated this situation and came up with correlations for the equivalent inner radius of the cylindrical shell to quickly calculate a

cone's heat conduction [54]. For more complex geometries, finite element analysis (FEA) is required [55].

For their theoretical estimates, Leenders H. [31] and Takken A. [8] ignore the heat conduction loss within the RAC and only consider it through the insulation material. This approximation undeniably simplifies the tool. Takken A. explains that this approximation is valid due to the material's high thermal conductivity and to support his claim, he further points out that all the temperature data points from Leenders H. are close. However, Leenders H. only measured outer wall temperature points, which differ by a maximum of around 40K, and it would be more relevant for the claim to have access to the inner wall temperature. Thus, more substantiation, such as FEA simulations or experimental data, is needed to fully back this assumption.

Nevertheless, conduction is taken into account if insulation is considered [8] [31]. Since the insulation's temperature is the one determining the outer temperature and, by extension, its outer radiation and convection loss, it is relevant to know how much heat is transferred to it. The conduction through the insulation is set equal to the power that is lost due to convection and radiation at the outside of the insulation:

$$Q_{ins,cond} = Q_{ins,rad} + Q_{ins,conv}. \quad (3.19)$$

By knowing the RAC's temperature, this relation can be solved numerically to determine the exterior losses.

It is relevant to note that, for lower mass geometries, the conduction heat loss is also lower since there is less material to conduct heat [34]. Thus, it might be advantageous to opt for such designs in cases where conduction heat is significant.

### 3.7. CONVECTION

Convection is the heat transfer mechanism related to the transfer of heat between a bounding surface and a fluid in motion or across the flow plane within the interior of the fluid. When the fluid motion is caused by, for example, a pump or a fan, it is called forced convection, and, when the fluid motion is caused by density differences due to temperature differences, it is named natural convection [56].

Convection is governed by Newton's law of cooling:

$$Q_c = h_c A \Delta T, \quad (3.20)$$

where  $Q_c$  is the rate of heat transfer,  $h_c$  is the convective heat transfer coefficient, and  $\Delta T$  is the temperature difference which depends on the situation [56]. The value of  $h$  can vary drastically depending on several factors such as geometry and temperature, and it can be calculated by:

$$h_c = \frac{Nu \cdot k}{L_s}, \quad (3.21)$$

where  $k$  is the fluid's thermal conductivity,  $L_s$  is the characteristic length which depends on geometry, and  $Nu$  is the Nusselt number [4]. There are several empirical relations to calculate  $Nu$  which depend highly on the scenario.

The RAC will experience natural convection in its inner cavity and outer wall. On the other hand, forced convection occurs inside the propellant tubes from the hot wall to the fluid.

### 3.7.1. INNER CAVITY CONVECTION

The heating of the cavity leads to convection heating of the fluid inside the cavity. In space, since there is a vacuum, this is no concern, however, on earth, this can only be avoided by using a vacuum chamber. This subject is a great concern in solar cavity receivers of parabolic dish-receiver systems and solar power tower [57] [58] and several formulas have been established with experimental and numerical data [59] [60]. However, most of the studies focus on downfacing angles as its the main situation in those scenarios and the formulas are not usually exact with margin errors of 50% [60]. The most relevant and simple conclusions from research are that the convection loss is highly dependent on the angle of the opening, the loss increases with the increase in the aperture and outer diameter ratio, and higher inner wall temperature [59].

A recent paper by Wang K. et al. performed a numerical study on the natural convective heat loss of an isothermal upward-facing cylindrical cavity [61]. In the paper,  $AR$  corresponds to the opening ratio,  $\phi$  to the angle (-90° means upward and 0° means sideways opening),  $Q_c$  the convection heat loss and  $T_w$  to the inner temperature. Regarding the effect of the inner temperature, there is a linear relationship between  $T_w$  and  $Q_c$  and the slope diminishes with  $AR$  decrease (fig. 3.10a) Natural convection heat loss is maximum at around -30° and is minimum at -90° which is explained by the higher velocity of inflow and outflow of air into the aperture (fig. 3.10b). Finally, concerning  $AR$ , it is clear that lower values lead to lower natural convection losses as the decrease in area obstructs the natural air flow (Fig. 3.10c).

From the results, an empirical relation to estimating  $Q_c$  in an open cylindrical cavity has been established. The Nusselt Number is calculated by:

$$Nu_D = 7.26 \times 10^{-5} Gr^{0.3533} [4 + \cos(\phi + 30)]^{5.8632} \left( \frac{A_{ap}}{A_{cav}} \right)^{1.0266}, \quad (3.22)$$

where  $A_{ap}$  is the aperture's area,  $A_{cav}$  is the heat transfer area (in this case, the cavity's inner wall), and  $Gr$  is the dimensionless Grashof number (ratio of the buoyancy to viscous forces acting on a fluid) and is calculated by:

$$Gr = \frac{g_0 \beta \rho^2 (T_w - T_\infty) D^3}{\mu^2}, \quad (3.23)$$

where  $g$  is the acceleration of gravity,  $\beta$  the fluid's thermal expansion coefficient,  $T_\infty$  the air's surrounding temperature, and  $D$  is the cylinder's diameter. Then the total heat loss by convection  $Q_c$  is:

$$Q_c = h_c A_{cav} (T_w - T_\infty) = \frac{Nu_D k}{D} A_{cav} (T_w - T_\infty). \quad (3.24)$$

It is relevant to mention that these equations are valid for  $-85^\circ \leq \phi \leq 0^\circ$ ,  $0.50 \leq AR \leq 1.0$ , and  $7.82 \times 10^5 \leq Gr \leq 1.94 \times 10^6$ . About 98.1% and 76.2% data points fluctuate within

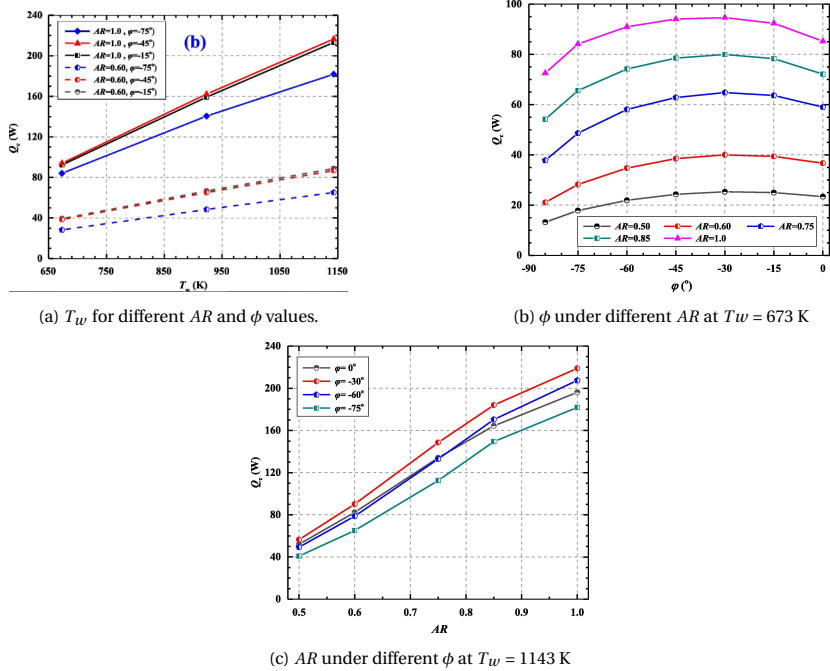


Figure 3.10: Variations of  $Q_c$  for a cylindrical cavity in different conditions [61].

$\pm 20\%$  and  $\pm 10\%$ , respectively, which indicates that the prediction accuracy of the correlation is fairly satisfactory [61].

Regarding conical-shaped cavities, there appears to not be much research available especially in upward-facing angles with no wind conditions. However, Jilte R. et. al [53] performed natural convection loss simulations with sideways as well as downward angles with several types of geometry, including cylindrical and conical shapes, in two distinct cases. In the first one, the heat transfer area was the same for all geometries, and, in the second one, the aspect ratio was equal (in this paper, defined as the ratio of the cavity's length and its aperture diameter). From the results displayed in figures 3.11a and 3.11b, it is clear that the conical-shaped cavity is always the shape with the lowest convection loss. Thus, with the assumption that this relative trend remains in upward-facing angles, the cone has lower convection heat losses than the cylinder. It is relevant to mention that, in this paper, the aperture ratio is unitary and an alternative value could possibly result in a different relation between the two geometries. From the data, a possibly fair estimate for the conical scenario seems to be calculating the convection loss with Wang K. et al. method [61] for a cylinder with an equal heat transfer area.

Takken A. [8] and Leenders H. [31] used a correlation method developed for open cavity receivers by Paitoonsurikarn S. et al. [62]. Despite being valid for conical and cylindrical shapes, it is only valid for side-ways orientation. Nevertheless, from Wang K. et al. [61], more specifically fig. 3.10b, the side-ways condition tends to result in a slightly higher convection loss and, thus, the method might determine a maximum loss value.

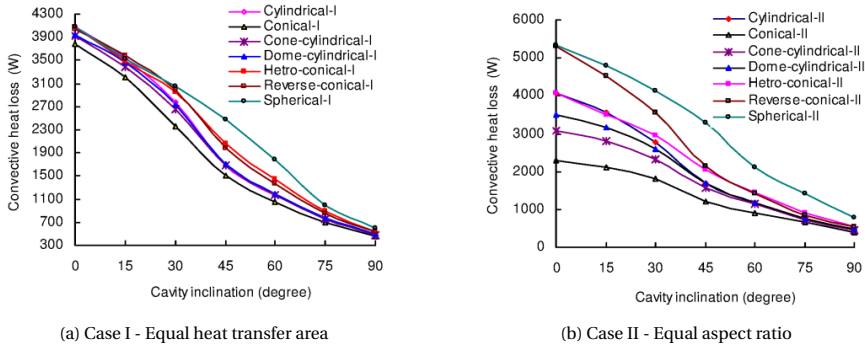


Figure 3.11: Convection heat loss for different geometries [53].

### 3.7.2. SINGLE-PHASE PROPELLANT CONVECTION

The heat transfer from the wall to the fluid is the main principle of the RAC and, thus, it is undeniably important concerning its performance. The wall's temperature  $T_w$  can be considered somewhat uniform throughout the propellant flow due to its high thermal conductivity [34]. Thus, from [34], the convective heat transferred  $Q_c$  as well as the final temperature, follow this relation:

$$Q_c = \bar{h}A \frac{(T_{p,f} - T_{p,i})}{\ln\left(\frac{T_{p,f} - T_w}{T_{p,i} - T_w}\right)} = \dot{m}c_p(T_{p,f} - T_{p,i}), \quad (3.25)$$

where  $\bar{h}$  is the mean convective heat transfer,  $A$  is the surface area,  $T_p$  is the propellant's temperature,  $\dot{m}$  is the mass flow,  $c_p$  is the propellant's specific heat capacity, and the subscripts  $i$  and  $f$  refer to initial and final conditions, respectively. The logarithmic mean temperature difference is present due to the decrease in the difference between the temperatures of the propellant and wall along the duct. A rearrangement of equation (3.25) leads to:

$$\frac{T_{p,f} - T_{p,i}}{T_w - T_{p,i}} = 1 - \exp\left(-\frac{\bar{h}PL}{\dot{m}c_p}\right), \quad (3.26)$$

where  $A$  was substituted by the multiplication of the tube's length  $L$  and its cross section's perimeter  $P$  to illustrate better their influence.

It is clear that  $\bar{h}$  highly influences the convective heat transfer and, from equation (3.21), it is dependent on the Nusselt number. However, before going directly to its formula, the Nusselt number depends on several variables which will be examined first.

#### Reynolds Number

The Nusselt number depends on the propellant's flow type: laminar, transitional or turbulent. That flow's characteristic is determined by the dimensionless Reynolds num-

ber  $Re$  which is the ratio between inertial forces to viscous forces, and it is given by the following equation:

$$Re_D = \frac{\rho u D}{\mu} = \frac{4\dot{m}}{P\mu}, \quad (3.27)$$

where  $\rho$  is the density,  $u$  is the velocity,  $D$  is the diameter,  $\mu$  is the dynamic viscosity and  $P$  is the perimeter.

Laminar flows are described by Reynolds numbers below 2300 whilst turbulent flow from Reynolds numbers of 10000 [34]. Turbulent flow has higher convection heat transfer than laminar flow and, thus, achieving that regime might be beneficial and can be done by increasing mass flow or diminishing the duct's perimeter. However, the propellant's velocity can not be too high as it can experience what is called water-hammer. Zandbergen [4] presents a formula to calculate its upper limit:

$$u_{max} = 175 \left( \frac{1}{\rho} \right)^{0.43}. \quad (3.28)$$

### Thermal entrance length and Prandtl Number

Another Nusselt number dependency is if the flow regime is fully developed. The flow can be hydro-dynamically developed (the velocity profile is constant along the duct) and thermally developed (the temperature profile is constant along the duct) [34]. It is important to notice that the flow can not be thermally developed without hydro-dynamical development.

The thermal entrance length is the section at the start of the pipe where the flow is not thermally developed and, therefore, the temperature profile is not constant, causing variations in the Nusselt number. For laminar flow, the thermal entrance length  $x_{e_t}$ , formula at a uniform wall temperature is [34]:

$$\frac{x_{e_t}}{D} = 0.034 Re_D Pr, \quad (3.29)$$

where  $Pr$  is the dimensionless Prandtl number which is the ratio between momentum diffusivity and thermal diffusivity [56]:

$$Pr = \frac{\mu c_p}{k}. \quad (3.30)$$

Regarding turbulent flow, there is no gratifying general equation for the thermal entrance length but it is generally accepted that it does not depend on the Reynolds number for enough large Prandtl numbers. Bergman T. et al. [63] provide a fair estimate:

$$\frac{x_{e_t}}{D} = 10. \quad (3.31)$$

Generally, the convective heat transfer is higher at the entrance region and the equations for the Nusselt number are averages throughout the whole pipe which take into account said region [63]. In an isothermal pipe, when the fluid is fully developed the Nusselt number is equal to:

$$Nu_D = 3.657. \quad (3.32)$$

Consequently, the formula for  $Nu_D$  is expected to converge to this value (from higher values) as the thermal entrance section becomes relatively smaller than the duct's length. In 1956, Sellars, Tribus, and Klein solved the problem of the constant wall temperature proposed by Graetz and discovered there is a useful dimensionless number to take into account the effect of the thermal entrance section - the Graetz number  $Gz$  - which is calculated by [34]:

3

$$Gz = \frac{Re_D Pr D}{L}, \quad (3.33)$$

where  $D$  is the duct's diameter and  $L$  is the length.

#### Hydraulic Diameter

The previous equations were all based on circular ducts and the Nusselt number is affected by the ducts' geometry. Nevertheless, all the previous thought process is still valid but the equations need to be adjusted. The hydraulic diameter  $D_h$  can be used to approximate the heat transfer coefficients in non-circular pipes [34]:

$$D_h = \frac{4A}{P}. \quad (3.34)$$

The results from this substitution in all the previous relevant formulas are usually within  $\pm 20\%$  and often within  $\pm 10\%$  and the worse results are generally present in sharp angle geometry such as acute triangles [34]. This accuracy can be improved by applying specific geometry equations that can be seen in [56].

#### Channel Layout

From previous work [8] [31] [39], the choice has been mainly between two different channel layouts: linear tubing or spiral tubing. In fact, this property influences as well the Nusselt number [4]. For its conical cavity, Leenders H. used linear tubing [31] while Takken A. chose spiral for its cylindrical cavity [8].

For the same cavity's length, spiral tubing has the advantage over linear tubing since it can increase its contact length. This increase in length can be varied as the spiralling angle can be changed. Furthermore, Rohsenhow W. et al. mention that spiral flow has a higher heat transfer due to a secondary flow induced by the presence of centrifugal forces. Consequently, spiral tubing is widely used in industry [56].

#### Surface Roughness

When the surface of a pipe is rough enough, it can disturb the thin layers of fluid near the surface that affect how heat and momentum transfer between the fluid and the pipe wall. As the fluid flow's Reynolds number increases, the thin layer closest to the surface becomes even thinner. At a certain point, the roughness of the pipe wall becomes more

important than this thin layer, and the friction between the fluid and the wall is mainly determined by the size of the roughness compared to the pipe diameter [34]. This is described by the roughness Reynolds number equation:

$$Re_\epsilon = \frac{\rho \epsilon u^*}{\mu}, \quad (3.35)$$

where  $u^*$  is the friction velocity and  $\epsilon$  is the material's roughness. The roughness Reynolds number tells us whether the roughness on the surface of the pipe will affect the friction and heat transfer between the fluid and the pipe. If it is less than 5, the pipe is considered to be hydraulically smooth; if it is greater than 70, the pipe is considered to be fully rough; and if it is between 5 and 70, the pipe is in a transitional state [34]. There are established relationships in scientific literature to predict the heat transfer [64] and friction properties [65] for fully rough pipes.

When the surface of a pipe is rough, it can increase the amount of heat transferred between the fluid and the pipe wall. However, it also increases friction, which results in higher pressure losses [34].

### Nusselt Number equations

As all the vital characteristics influence the Nusselt number in the relevant scenario, it is possible to present the equations that calculate it. Several fluid properties like viscosity and density depend on the fluid's temperature and, therefore, they should be taken at meaningful temperatures. The most appropriate temperature is the mean temperature between the fluid's initial and final temperature, however, the final temperature is not initially known. Consequently, a strategy can be to take the properties at the mean temperature between the propellant's initial temperature and the wall's temperature and calculate its final temperature. Another possibility is to use only the initial temperature as a reference. After getting the first final temperature value, performing at least one iteration is recommended through the same formulas again with the properties at the fluid's mean temperature since now there is an initial estimate for the final temperature's value. Through several iterations of this method, the final temperature value should converge.

Concerning laminar flow in linear ducts, for an isothermal wall, the Nusselt number is calculated by [34]:

$$Nu_D = \frac{3.657}{\tanh(2.264Gz^{-\frac{1}{3}} + 1.7Gz^{-\frac{2}{3}})} + 0.0499Gz\tanh(Gz^{-1}) \quad (3.36)$$

As the length increases, the Graetz number tends to zero and the Nusselt number tends to 3.657 as expected previously.

In regards to turbulent flow in linear ducts, the Gnielinski equation is the most widely used [66] and is valid for a wide range of values. In fact, this range is not consensual as different sources state different ranges. A recent source by Lienhard J. et. al [34] mentions the range to be  $2300 \leq Re_D \leq 5 \times 10^6$  and  $0.6 \leq Pr \leq 10^5$ . However, the original Gnielinski equation does not take into account the thermal entrance region which can be crucial at small duct lengths. Taler D. et. al [67] modified the equation usefully by multiplying the original with a term that tends to one as the length increases:

$$Nu_D = \frac{\left(\frac{f_{DB}}{8}\right)(Re_D - 1000)Pr}{1 + 12.7\sqrt{\left(\frac{f}{8}\right)}(Pr^{\frac{2}{3}} - 1)} \left(1 + \left(\frac{D}{L}\right)^{\frac{2}{3}}\right). \quad (3.37)$$

where  $f_{DB}$  is the dimensionless Darcy-Weisbach friction factor whose calculation is explained further in section 3.8.

Regarding flow in spiral tubes, Ferreira [10] gathered for his thesis a collection of useful formulas for the Nusselt number. Later, Takken [8] also uses the same equations. It is relevant to understand that each formula is applicable within its defined conditions.

3

### 3.7.3. TWO-PHASE PROPELLANT CONVECTION

Under certain conditions, the liquid may reach its saturation point and undergo flow boiling, resulting in a two-phase mixture of liquid and vapour. In this scenario, heat transfer occurs through both convective heat transfer and nucleate boiling and the heat flux is primarily used for evaporation [68]. The extra interaction between two different fluid phases usually leads to a higher convection heat transfer [34]. In fig. 3.12, it is possible to visualize the different flow patterns in a two-phase boiling flow.

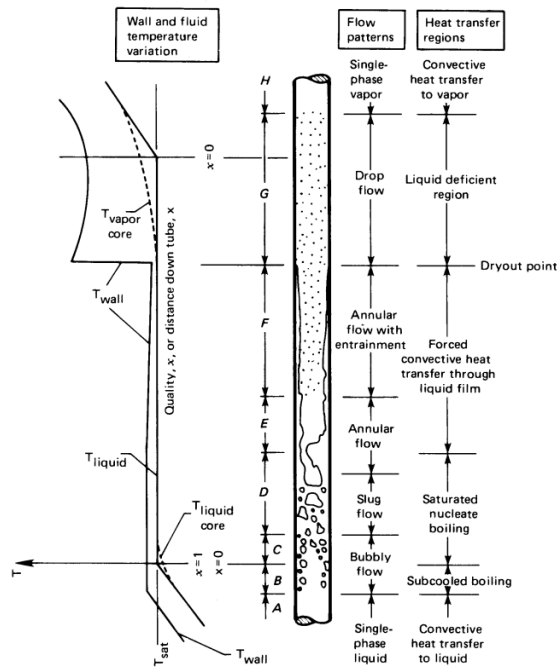


Figure 3.12: The development of a two-phase flow in a vertical tube with a uniform wall heat flux (not to scale) [34]

Several equations have been developed to predict heat transfer in this case. However, in the literature, the majority studies the constant wall heat flux scenario. For example,

Lienhard J. et al. [34] calculate the heat transfer for the nucleate boiling dominant and the convective boiling dominant cases and choose the biggest; the equations depend on the dimensionless boiling number which depends on the wall's heat flux.

The boiling curve of water at 1 atm can be seen in fig. 3.13. Boiling curves allow us to determine in which type of heat transfer regime the flow is considered the temperature difference between the fluid and the wall.

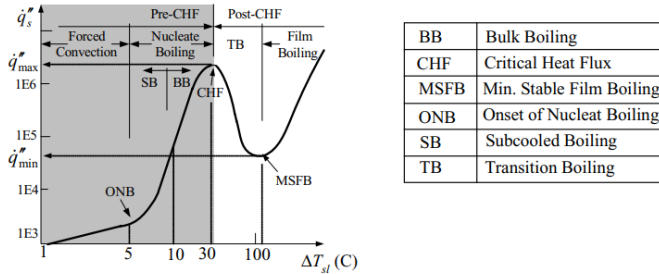


Figure 3.13: The boiling curve of water at 1 atm and various heat transfer regimes [68]

Additionally, the heat transfer regime determines the set of equations to estimate the heat transfer process [68]. For instance, regarding film boiling, which is certainly the case when the propellant is hydrogen, Massoud M. [69] suggests the Dougal-Rohsenow correlation:

$$h = 0.023 \frac{k}{D} \left( Re \frac{\rho g}{\rho} \right)^{0.8} Pr^{0.4}. \quad (3.38)$$

Concerning spiral ducts, there seems to be a lack of trustworthy correlations in the literature. Consequently, the linear case is used.

### 3.7.4. OUTER WALL CONVECTION

With the RAC's outer wall having a higher temperature than the surrounding medium, natural convection also occurs which induces energy losses. The geometry, as usual, also influences the amount of heat lost by convection of the outer wall [56]. Unfortunately, no information was found regarding outer convection loss in open cavities, only closed surfaces. Nevertheless, these closed surface formulas can give an irrefutably useful approximation which is better as the aperture ratio is smaller.

Rohsenow W. et al. [56] give formulas for several geometries including short vertical and horizontal cylinders and horizontal cones. In fact, Leenders H. [31] also used these equations. However, it requires the calculation of several quantities and the use of tabulated values which depend on the limited available length-to-diameter ratio. Therefore, it is a complex process.

However, simpler relations exist which do not require tabulated values in literature. Oosthuizen P. experimentally investigated free convective heat transfer from horizontal cones [70]:

$$Nu_D = 0.7 + 0.35Ra_D^{0.125} + 0.51Ra_D^{0.25}, \quad (3.39)$$

where  $Ra_D$  is the Rayleigh number:

$$Ra_D = Gr_D Pr. \quad (3.40)$$

The same author also published an article for the free convective heat transfer from vertical cones [71], where the following equation is obtained:

$$Nu_l = 0.65 \left( Gr_l^{0.25} + \frac{1.44}{\tan\left(\frac{\phi}{2}\right)} \right), \quad (3.41)$$

where  $Gr$  is the Grashof number and  $\phi$  is the cone's included angle. In this case,  $Nu_l$  and  $Gr_l$  are based on the cone's slant height. These equations are simpler than the previous ones as they entail fewer equations and no dependency on tabulated values.

Regarding the cylinder, Churchill S. and Chu H. [72] present the following equation in the horizontal case:

$$Nu_D = \sqrt{0.6 + 0.387 \left( \frac{Ra_D}{\left( 1 + \left( \frac{0.559}{Pr} \right)^{\frac{9}{16}} \right)^{\frac{16}{9}}} \right)^{\frac{1}{6}}}. \quad (3.42)$$

For the vertical case, Day J. et al. [73] performed numerical simulations and achieve formulas for cylinders with a length-to-diameter ratio from 0.1 to 10. For example, the formula applicable when the ratio is between 2 and 10 is:

$$Nu_L = -0.06211 + 0.54414 Ra_L^{\frac{1}{4}} + 0.6123 \frac{L}{D}. \quad (3.43)$$

The formula for 0.1 to 2 is of a similar structure, only the coefficients change.

The resulting Nusselt number is an average for the whole outer surface and, thus, in equation (3.20),  $A$  corresponds to the outer surface area minus the aperture area to approximate the cavity's scenario.

### 3.8. PRESSURE GRADIENT

Pressure gradients refer to the change in pressure that occurs in a fluid as it flows through a pipe. The pressure gradient is caused by various factors, such as fluid viscosity, pipe geometry, flow rate, and external forces like gravity [34]. Since the nozzle is designed for a certain chamber pressure [4], it is ideal to know the pressure drop between the propellant tank to the chamber in order to understand at what pressure the propellant needs to be stored or vice-versa. There are different types of pressure gradients which will be discussed further and their sum is equal to the total gradient.

[Single-phase flow friction pressure gradient](#)

The pressure loss due to friction in a single-phase flow is easily calculated by the Darcy-Weisbach equation [34]:

$$\Delta p_{sp} = f_{DB} \frac{L}{D} \frac{1}{2} \rho u^2, \quad (3.44)$$

where  $sp$  stands for single-phase,  $L$  and  $D$  are the tube's length and diameter, respectively,  $\rho$  and  $u$  is the propellant's density and velocity, and  $f_{DB}$  is the dimensionless Darcy-Weisbach friction factor. For laminar and turbulent flow in linear smooth pipes, the friction factor is calculated, respectively, by [34]:

$$f_{DB} = \frac{64}{Re_D}, \quad (3.45a)$$

$$f_{DB} = \frac{1}{(1.82 \log Re_D - 1.64)^2}. \quad (3.45b)$$

On the other hand, for rough pipes, it is advised to consult a Moody diagram to extract values. Regarding spiral ducts, their friction factor is higher than linear and Guo L. et al. [74] recommend the following relationships for, respectively, laminar and turbulent flow:

$$f_{DB} = \frac{1}{1 - \left( 1 - \left( \frac{11.6}{Re_D \left( \frac{D}{D_c} \right)^{0.5}} \right)^{0.45} \right)^{\frac{1}{0.45}}} \frac{64}{Re_D}, \quad (3.46a)$$

$$f_{DB} = 0.304 Re_D^{-0.25} + 0.029 \left( \frac{D}{D_c} \right)^{0.5}, \quad (3.46b)$$

where  $D_c$  is the diameter of the spiral.

#### Two-phase flow friction pressure gradient

The friction loss in two-phase flow is similar to the single-phase scenario. In fact, it is the same formula multiplied by a coefficient named the two-phase multiplier  $\phi$ :

$$\Delta p_{tp} = \phi \Delta p_{sp} = \phi f_{DB} \frac{L}{D} \frac{1}{2} \rho u^2. \quad (3.47)$$

Several correlations for  $\phi$  have been proposed with some being more complex than others, usually emerging from experimental test data. Massoud M. [69] mentions several equations such as the Reddy as well as the Friedel correlation. For horizontal and slightly inclined straight tubes, the Lockhart-Martinelli correlation [75] is commonly used in industry. Concerning helically coiled pipes, Guo L. et al. [74] proposed a correlation based on their own experimental data, however, prediction values can still diverge by about 40%. Gravity influences the pressure drop: horizontal tubes have the lowest value while the 45° downwards inclined coil has a 70% increase and the 45° upwards is in between these two values [74].

Experimental data concerning two-phase boiling flow in microgravity conditions is scarce as well as reliable correlations [76]. Consequently, it is better to consider the correlations obtained in earth-gravity conditions.

### Acceleration pressure gradient

The acceleration pressure gradient  $\Delta p_{ac}$  results from a change of density and cross-section [77]:

3

$$dp_{ac} = \frac{\dot{m}}{A} du = Gd\left(\frac{G}{\rho}\right), \quad (3.48)$$

where  $G$  is the flow rate. Depending on the scenario, the equation can be simplified. For example, in a single-phase flow with a constant cross-section area:

$$\Delta p_{ac,1-2} = G^2 \left( \frac{1}{\rho_2} - \frac{1}{\rho_1} \right). \quad (3.49)$$

In two-phase flow, the previous equation applies if a full transition from liquid to gas occurs:  $\rho_2$  being the gas density and  $\rho_1$  being the liquid density. In the general scenario for variable cross-section, the following formula applies:

$$dp_{ac} = \frac{1}{A} d \left( A \left( \frac{G_g^2}{\alpha_v \rho_g} \right) + \left( \frac{G_l^2}{(1 - \alpha_v) \rho_l} \right) \right), \quad (3.50)$$

where  $\alpha_v$  is the void fraction which is the gaseous volume fraction.

### Gravitational pressure gradient

As the fluid moves downwards a pipe, the pressure at any given point will be influenced by the height of the fluid column above that point. The pressure at the bottom of the pipe will be greater than the pressure at the top of the pipe due to the weight of the fluid in the column and is calculated by [69]:

$$\Delta p_{grav} = \rho g_0 \sin \gamma, \quad (3.51)$$

where  $\gamma$  is the inclination of the pipe (positive if flowing downwards and negative otherwise). Thus, the pressure gradient due to gravity will cause the pressure to decrease as the fluid flows upward against gravity, and increase as the fluid flows downward with gravity [34].

## 3.9. WALL THICKNESS

As mentioned previously, lower mass geometries are desired to reduce the conduction heat losses. In fact, this can be done by reducing the thickness of the RAC walls. However, it is also necessary to guarantee that the RAC can withstand the pressure and thermal stresses during operation and, thus, a minimum wall thickness is required.

Concerning regular pipes, Barlow's equation [78] is commonly used to ensure that the pipe's thickness  $t$  is enough to withstand its internal pressures:

$$t = \frac{p_{int} D_{out} j}{2\sigma}, \quad (3.52)$$

where  $p_{int}$  is the internal pressure,  $D_{out}$  is the outer diameter,  $j$  is the safety factor and  $\sigma$  is the allowable stress of the material. The safety factor value depends on the situation and typical values are between 1.25 and 2 [4].

In his thesis, Preijde J. [39] uses Barlow's equation to ensure the structural integrity of the pipes. However, the RAC is made of several adjacent ducts and not a single one which is the case of that correlation. Furthermore, the RAC suffers from a high thermal load which increases the possible structural failure. In more complex geometries, finite-element analysis (FEA) is recommended to identify minimum wall thickness values. In addition, it allows taking into account the thermal load. In the literature, several authors use this method for the mentioned purpose [79] [80].

3

## 3.10. RAC TOOL

Considering the previous information gathered from the literature, a simple Matlab model was built to predict the RAC's performance.

The tool's inputs are the laser output power and the fraction of it that is absorbed by the RAC, ambient temperature, the RAC (material, dimensions, emissivity, mass and if conical or cylindrical), the pipes (number, if spiral or linear, dimensions and length), and the propellant (initial temperature and pressure, and mass flow). Consequently, the relevant outputs are the RAC's and propellant's final temperature as well as total pressure loss. Concerning the propellant properties, these are extracted from the NIST Webbook by a web scraper.

The fundamental process of the tool is quite simple. Considering the initial temperatures, the radiative and conductive losses are easily calculated as they follow direct formulas identified from the literature and depend only on the RAC geometry. On the other hand, the heat transfer to the propellant is more complex. A first estimate for the propellant final temperature is made assuming single-phase flow throughout the whole pipe. Afterwards, it is determined if somewhere within the duct the fluid reaches boiling temperature. If not, then the first estimate is the final result. Otherwise, the point where the boiling starts is determined by the bisection method. As soon as it is determined, the heat transferred to the fluid for the remainder of the pipe is calculated with the two-phase flow equations. Then, the heat is compared to the required energy to fully evaporate the fluid. If it is not enough, then the final temperature is the previous, otherwise, again, the point where the fluid finishes evaporating is calculated by the bisection method. The remainder of the pipe length is used in the single-phase flow equations to calculate the final temperate. Now with all the heat transfer calculated, the RAC's temperature is updated taking into account the transient heat equation. With the new RAC temperature, the mentioned process repeats until the equilibrium temperature is reached.

Verification of the tool was performed by varying inputs and comparing the results with expected values and trends. For instance, reducing mass flow or increasing laser input resulted in higher propellant temperatures. Unfortunately, most sources in the literature do not provide enough design information to perform the predictions by the tool.

Nevertheless, the values from Preijde J.'s tool and Leenders H.'s experimental were used and compared. From the results (table 3.4), it is undeniable that the thermal model provides similar results to both the model from Preijde J. and Leenders H.'s experiment. The differences might be caused by the fact that in the other model, the propellant tubing is not incorporated into the cavity and extra thermal elements are present; whereas, in the experiment, surface roughness or other irregularities might have increased the heat transfer to the fluid. Nevertheless, the closeness of the results leads to the validation of the current tool.

## 3

Table 3.4: Comparison of model and experimental results

Temperature (K)	Model	Preijde	Leenders
Max Cavity	656	652	650
Final Cavity	518	522	525
Max Propellant	502	489	525
Final Propellant	443	420	477

# 4

## NOZZLE

In the nozzle, the high-temperature gas produced by the laser heating is converted into thrust and its design is important to maximize the efficiency and performance of the propulsion system. Firstly, relevant physical quantities and efficiencies related to thruster performance are introduced. Next, nozzle geometry is discussed. Lastly, the ideal rocket theory is mentioned succinctly, as well as, phenomena that negatively affect the performance and how they are estimated.

### 4.1. QUANTITIES AND EFFICIENCIES

Thrust is an important measure of the performance of a propulsion system. Thrust is the force that propels a spacecraft forward, in the opposite direction to the exhaust gas flow from the propulsion system and can be calculated by:

$$F = \dot{m}U_{eq}, \quad (4.1)$$

where  $\dot{m}$  is the mass flow and  $U_{eq}$  is the equivalent exhaust velocity relative to the vehicle:

$$U_{eq} = U_e + \frac{p_e - p_{amb}}{\dot{m}} A_e, \quad (4.2)$$

where  $U_e$  is the exhaust velocity,  $p_e$  and  $p_a$  are, respectively, the nozzle exit pressure and ambient pressure, and  $A_e$  is the nozzle's exit area. Thrust determines the vehicle's acceleration and, therefore, the greater the thrust, the faster a spacecraft can accelerate and reach its destination [4]. The maximum thrust is achieved when  $p_e$  and  $p_{amb}$  are equal.

Another relevant quantity is the propellant-specific impulse which is defined as the thrust produced per unit of propellant consumed. Consequently, it is a measure of efficiency, since higher specific impulses lead to less propellant consumption for the same thrust and result in less propellant to be carried for a certain mission [4] and it is calculated by:

$$I_{sp} = \frac{U_{eq}}{g_0}, \quad (4.3)$$

where  $g_0$  is the gravitational acceleration at sea level. Thus, it is only dependent on the propellant's exhaust velocity which is dependent on the propellant and the nozzle design.

It is relevant to note that increasing the specific impulse of the system does not necessarily lead to higher thrust. Even though thrust also depends on the exhaust velocity, the exhaust velocity can be increased by reducing the mass flow, for example, which can lead to a thrust decrease. Nevertheless, for a given mass flow, the nozzle shape can be optimized to increase both quantities by improving the exhaust velocity.

Thrust efficiency is determined by how well the thruster converts the input power into jet power  $P_J$  (defined as the kinetic power in the jet). In this case, the input power can be considered the RAC power input into the propellant and is then calculated by:

$$\eta_T = \frac{P_J}{P_{prop}} = \frac{\frac{1}{2} \dot{m} U_{eq}^2}{P_{prop}}. \quad (4.4)$$

The higher the thrust efficiency, the less power is needed by the propulsion system to produce a certain jet power [4].

The power provided by the rocket should be transferred into mechanical power. A measure of how efficiently this occurs is given by the rocket efficiency. It can be calculated from:

$$\eta_R = \frac{F \cdot v}{\frac{1}{2} \dot{m} (v - U_{eq})^2 + F \cdot v}, \quad (4.5)$$

where  $v$  is the rocket's flight velocity. the first term in the denominator is the absolute kinetic power in the exhaust jet [4].

## 4.2. GEOMETRY

The nozzle typically consists of a converging section, a throat, and a diverging section (fig. 4.1). The converging section reduces the diameter of the exhaust gas flow, increasing the gas velocity and kinetic energy. The throat is the point of maximum constriction in the nozzle, where the gas velocity is highest and the pressure is lowest. The diverging section then gradually increases the diameter of the exhaust gas flow, allowing the gas to expand and convert its high kinetic energy into thrust [4].

The divergent section has many shapes (fig. 4.2) and the most common are the conical and the (ideal or truncated) bell. The conical nozzle, while simple to make and inexpensive, suffers from flow divergence losses and requires a lengthy nozzle to achieve a desired area ratio. This length can result in weight, space, and increased friction and heat transfer. The bell nozzle, on the other hand, minimizes flow divergence to nearly zero, but an ideal bell nozzle would require excessive length, leading to the same disadvantages as the conical nozzle. Therefore, truncated bell nozzles are used instead. More detail on the mentioned losses will be given in the following section.

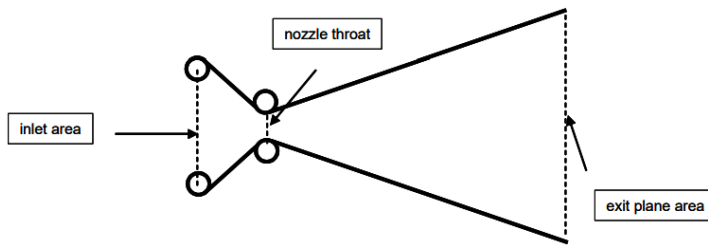
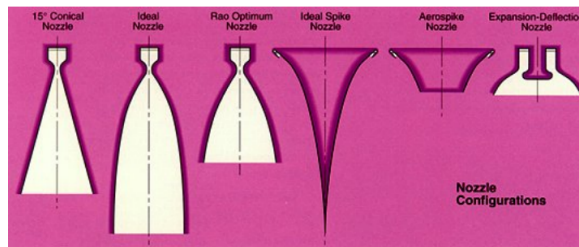


Figure 4.1: Nozzle Shape [4].



4

Figure 4.2: Typical nozzle shapes [4].

In a low-budget experimental setup, a conical nozzle might be the best choice due to its lower complexity which can reduce costs. Additionally, with the experimental data, one could estimate the performance of substituting it with a bell-shaped one.

### 4.3. IDEAL ROCKET THEORY

Ideal rocket theory is a theoretical framework used to model and analyze the performance of rockets based on fundamental principles of physics and engineering. Zandbergen's work [4] is a good and concise source to go deeper into the subject.

By knowing the propellant conditions at the chamber, it is possible to calculate the throat's required area  $A_t$ :

$$A_t = \frac{\dot{m} \sqrt{RT_c}}{\Gamma p_c} \quad (4.6)$$

where  $R$  is the specific gas constant,  $\Gamma$  is the Vandenkerckhove function, which depends only on the specific heat ratio  $\gamma$ , and  $T_c$  and  $p_c$  are the temperature and pressure, respectively, in the chamber.

Afterwards, there is a relation between the nozzle exit area and throat area (hereby defined as expansion ratio) and the ratio between the exit pressure and chamber pressure. Thus, it is possible to calculate the required nozzle exit area for a defined exit pressure or vice-versa. A large pressure drop is obtained with a high expansion ratio.

The exhaust velocity  $U_e$  can be calculated by:

$$U_e = \sqrt{2 \frac{\gamma}{\gamma-1} \frac{R_A}{M} T_c \left( 1 - \left( \frac{p_e}{p_c} \right)^{\frac{\gamma-1}{\gamma}} \right)}, \quad (4.7)$$

where  $R_A$  is the absolute gas constant and  $M$  is the propellant's molar mass. Consequently, for instance, higher  $U_e$  can be achieved with higher  $T_c$  and lower propellant  $M$  as mentioned several times before.

The Poisson equations are a set of equations which relate quantities such as pressure, temperature and density in an adiabatic process. At critical conditions (sonic flow at the throat), density, pressure and temperature ratios between the chamber and throat conditions follow these relations:

$$\left( \frac{p_t}{p_c} \right)_{cr} = \left( \frac{T_t}{T_c} \right)_{cr}^{\frac{\gamma}{\gamma-1}} = \left( \frac{\rho_t}{\rho_c} \right)_{cr}^{\gamma} = \left( \frac{2}{\gamma+1} \right)^{\frac{\gamma}{\gamma-1}}. \quad (4.8)$$

It is relevant to note that the relations between the ratios are always true in adiabatic conditions and that only the last value is based on the critical condition. Also, the critical velocity  $U_c$  is calculated by:

$$U_c = \sqrt{\gamma R T_t} \quad (4.9)$$

#### 4.4. CORRECTION FACTORS

The previous equations use ideal rocket theory to estimate the thruster's performance. However, real nozzles are characterized by greater complexity as they are subject to several factors which are not taken into account in ideal rocket theory and affect its performance. For instance, the divergence of the flow in the nozzle exit sections may result in varying losses, which depend on the cosine of the divergence angle; lower velocities at the wall boundary layers can reduce the effective average exhaust velocity by 0.5 to 1.5%; and unsteady combustion and flow oscillations can also lead to minor losses [81]. Additionally, combustion-related and heating loss-related correction factors are present [4].

For example, Takken A. [30], to account for this fact to some degree, mentions the discharge coefficient  $C_d$ :

$$C_d = \frac{\dot{m}_{real}}{\dot{m}_{ideal}}, \quad (4.10)$$

which relates the real mass flow with the ideal mass flow. This is most relevant when the throat's Reynolds number is below 10000 and a laminar boundary layer forms. Takken A. uses the correlations between the discharge coefficient and the Reynolds number published by Johnson et al. [82]. However, only four gases were studied: nitrogen, hydrogen, argon and carbon dioxide. Only the first two are of interest and for other propellants, no information is given.

On the other hand, Preijde J. [39] focuses on thrust losses due to flow divergence and the boundary layer. From the work of Berton J. [83], in conical nozzles, the first

component is considered by:

$$c_{divloss} = \frac{1 + \cos\theta_{div}}{2}. \quad (4.11)$$

Whereas, for bell-shaped nozzles, even though no equation is given, from the data given in [81], Preijde J. came up with:

$$c_{divloss} = 0.99 \frac{1 + \cos(\theta_{div} - \theta_{exh})}{2}. \quad (4.12)$$

Regarding the presence of boundary layer, the momentum thickness  $\theta_{mom}$  is calculated by [84]:

$$\theta_{mom} = 0.664 \frac{\sqrt{\mu x_l}}{U_e}, \quad (4.13)$$

where  $x_l$  is the total length of the diverging edge. Next, the loss in thrust is calculated by [85]:

$$F_{boundloss} = \theta_{mom} \rho_e U_e^2 2\pi R_e, \quad (4.14)$$

where  $R_e$  is the radius of the nozzle exit. Consequently, the real thrust is [81]:

$$F_{real} = c_{divloss} \dot{m} U_e + (p_e - p_a) A_e - F_{boundloss}. \quad (4.15)$$

No source in the literature was found that related these two different approaches, thus, combining them might not be correct. Concerning estimates, in the case of hydrogen and nitrogen, whose discharge coefficients are given [82], the mass flow in the previous equation is the real mass flow. The flow divergence at the exit is unrelated to the boundary layer formed in the throat and, therefore, it is always accounted for. On the other hand, the diverging edge's boundary layer loss might not be entirely independent of the discharge coefficient and, consequently, also using it might lead to even lower values than reality. Regarding propellants whose discharge coefficients are unknown, the flow divergence and boundary layer loss are considered and the mass flow used is the ideal one.

It is important to note that these approximations to real nozzles are not always accurate as they are based on certain assumptions which might not hold. Nevertheless, they still manage to predict to some useful degree the performance of the thruster.

## 4.5. NOZZLE TOOL

A nozzle tool was written in Matlab taking into account the previously mentioned ideal rocket theory as well as the correction factors. It is irrefutably simpler than the RAC Tool. The inputs are the propellant and its chamber conditions, and the nozzle shape (conical or bell-shaped). The outputs are the thrust (ideal and real) and specific impulse. Verification was performed in the same manner: varying inputs and comparing the results to expected values and trends. Validation was performed by comparing the results to the ones from Takken A. [8] and Preijde J. [39]. The ideal values change slightly (within 5%) and this is thought to be due to the propellant properties. The other tools do not seem to

extract the data directly from NIST but rather use a few data points and interpolate from them. Regarding the thrust correction process, the method explained in the previous section is used.

# 5

## PROPELLANT SYSTEM

The propellant, propellant tank, feed system, and tubing are all critical components of a rocket engine, including laser thermal space propulsion systems. Firstly, in this chapter, structural components such as the propellant tank and the tubing are discussed. Next, several propellant choices are mentioned as well as their advantages and disadvantages according to the literature.

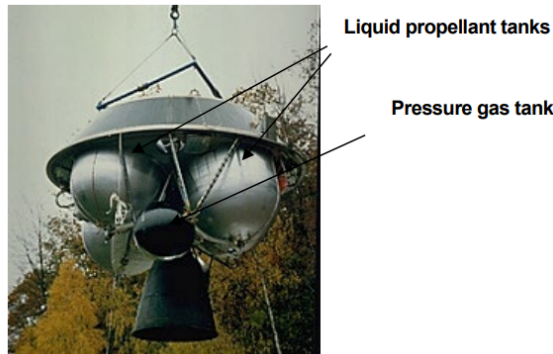
### 5.1. STORAGE AND FEEDING SYSTEM

For any liquid or cold gas propulsion system, a storage system is necessary. This system serves two fundamental purposes: to store the necessary fluids for propulsion and to maintain their usability. Nonetheless, the use of a storage system also presents certain drawbacks related to the weight, dimensions, expense, and dependability of the overall system [4]. For instance, for the Ariane 5 L9.7 upper stage (EPS) the tankage system makes up roughly 35% of the total stage dry mass [86]. Thus, techniques to reduce tanking mass have been developed. In addition, other important aspects that are taken into account are limiting its volume, limiting boil-off and preventing tank failure [4]. Laser thermal propulsion provides an advantage in this sector since only one propellant tank is required which reduces the weight.

Regarding their shape, spherical and cylindrical tanks are most common in space-craft propulsion systems [4]. The former is due to it being the optimal shape as it results in the lowest mass, whilst the latter is preferred to use the available volume in a more advantageous manner. The material of the tank depends on the propellant stored but examples include aluminium, titanium, and more recently pre-stressed composites [4].

Furthermore, depending on the propellant and its storage conditions, insulation, refrigeration or a heater system might be required [4]. In long-duration cryogenic storage, the propellant boils off and insulation is used to diminish this. Also, extra propellant is required to account for this effect. Refrigeration systems are used to limit boil-off losses as well. On the other hand, a heater system may be needed to prevent freezing for propellants such as hydrazine.

There are two main distinctions when discussing feed systems: pressurized tank (fig. 5.1) and pump-fed. The latter, as the name states, uses a pump to feed the propellant from its storage to the propulsion system, while the former uses a pressurized gas in combination with another component to force the propellant out of the tank [4]. The pressurized gas can be stored inside the propellant tank, increasing its dimensions and, thus, mass, or stored in another tank, increasing the system's complexity.



5

Figure 5.1: Ariane 5 Aestus stage [4].

Regarding the total mass and volume of the storage and feeding system, Zandbergen B. [4], in his "Design of fluid storage system" chapter, goes into great detail and provides useful and fundamental equations for it. Takken A. [8] and Preijde J. [39] used this information to create their feed system tools as well as to justify some of their design choices. No more detail is given in the literature study regarding this subject as it does not concern any main objectives of the future thesis.

There is no defined efficiency for the propellant system as a whole. Pressure drops along the tubing are a concern that can be minimized but it is not dependent directly on, for instance, the pressure in the propellant tank and, thus, does not make sense to relate the drop to the total pressure. Other aspects such as boil-off loss reductions are hardly quantifiable in simple terms and, thus, there is no reason to discuss them in terms of efficiency.

## 5.2. PROPELLANT

In laser thermal propulsion, the propellant is the fluid that goes through the propulsion system and whose temperature is increased by the laser energy, producing the high-temperature exhaust gas that generates thrust. In this section, the proposed propellants throughout the literature are mentioned as well as the conclusions drawn by the authors.

The most commonly mentioned and analyzed propellants are hydrogen, ammonia, water, nitrogen and helium.

Liquid hydrogen is the most attractive candidate due to its low molar mass which entails the highest possible  $I_{sp}$ . However, hydrogen has a low melting point, putting it in the cryogenic storage area, and should be handled carefully due to its reactivity. The

latter makes it, generally, not possible for testing due to safety reasons.

Next, ammonia is attractive due to its low specific heat capacity, dissociation at high temperatures, high specific impulse and better storage than hydrogen. This propellant has been studied, for instance, by Leverone F. [7], Preijde J. [39] and Pino D. [24].

Water's major advantage is that it is greatly accessible. However, its performance is not the best; Preijde J. [39] mentions that water achieves too low temperatures, requires too much energy to vaporize and has too high storage volume, and its freezing point would require an additional heating system. Nevertheless, Leverone F. [7] states that water, for the same  $\Delta\nu$ , requires less storage volume than ammonia, making it more volumetrically attractive.

Gaseous nitrogen has been used experimentally due to its high availability and inert nature by, for instance, Leenders H. [31] and proposed by Takken A. [8]. Its performance is nowhere near the previous propellants and thus it is mostly ignored in theoretical work.

Lastly, helium has not been mentioned in previous students' work, however, it has been used in experimental research [87] [88]. In fact, helium is an inert gas and the element with the second lowest molar mass making it a potentially attractive experimental propellant to achieve high performance.

Consequently, for experimental thesis work on the subject, the options are quite limited because of safety reasons and the difficulties adjacent to the use of cryogenic propellants. Thus, three clear options remain water, nitrogen and helium. Water and nitrogen are easily obtained through the faculty [30], whereas helium might not be available and require outsourcing. Water is an interesting propellant as it allows to test for two-phase flow, a condition present in the liquid hydrogen case. Helium would allow performing experiments with performance more similar to hydrogen. Consequently, if possible, experimentation with these three propellants would result in a significant amount of data and interesting results.

# 6

## EXPERIMENTAL RESEARCH

Theory alone does not build rocket engines. Experimental tests and analysis are crucial for any scientific concept's development and laser thermal propulsion is in no way an exception. Since the testing of a laser thermal propulsion system in a laboratory is one of the goals of the following master's thesis, research regarding such experiments is mandatory. Thus, this chapter focuses on the experimental research found in the literature related to laser thermal propulsion as well as any other area that shares characteristics such as solar thermal propulsion.

### 6.1. LASER THERMAL EXPERIMENTS

In this section, experiments regarding laser thermal propulsion using indirect propulsion are briefly described and commented on. Unfortunately, there are few available experiments on this theme in the literature. Only recent papers from Japanese university research were found. Nevertheless, these experiments might be useful during the thesis.

Firstly, Eguchi K. et al. [88] performed experiments using helium with a porous carbon heat exchanger. The experimental setup is displayed in fig. 6.1. It consists of a chamber, nozzle, pressure vessels, heat exchanger, and optical window. The variables of the experiment were mainly the laser power, the porosity of the porous carbon and the helium's mass flow. Regarding measurements, only one pressure sensor is used on the side of the chamber and a load cell is used to measure the impulse. No temperature measurements are made and the temperature is calculated via the choke mass flow equation. A direct temperature measurement would be irrefutably beneficial as the value calculated is only a theoretical estimate based on certain assumptions which might not entirely hold. From the experimental data, a temperature of 1500K was achieved with the maximum laser output (4kW) and porosity (99.9%). However, efficiency, in that case, was only 20%. The main energy loss source was the radiation from the heated porous carbon whose effective area of emission was more than double its cylindrical surface. Additionally, the nozzle was poorly designed as the thrust coefficient was half of the optimum expansion value.

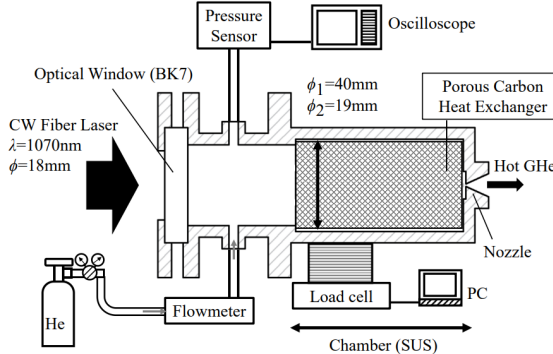


Figure 6.1: Eguchi's schematic of the experimental equipment [88]

In 2022, Mori [87] performed another similar experiment whose setup is displayed in fig. 6.2. In this experiment, the porosity of the porous carbon remained the same, the laser intensity was limited by the quartz-glass-tube temperature requirements and the maximum laser power delivered to the tissue surface was 500 W. Furthermore, two propellants, nitrogen and helium, were used. Compared to the previous setup, this setup has an additional pressure sensor as well as a temperature sensor before the nozzle which is an undeniable improvement. However, no impulse or thrust measurements are made. Comparing the experimental results to the theoretical ones, one of the reasons for the discrepancy is attributed to temperature non-uniformity as the temperature of the porous carbon is higher in its centre, where the thermocouple is located. Nevertheless, the findings suggest that at a high Reynolds number of around 10, the laser power is effectively transferred to the gas enthalpy.

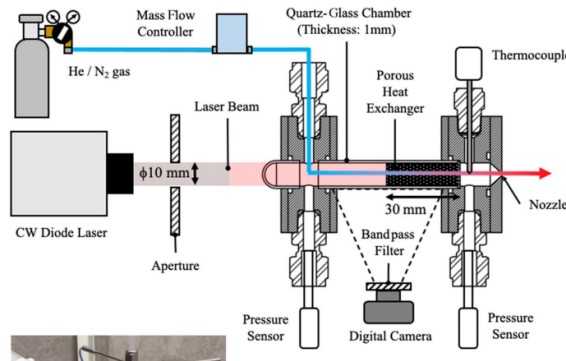


Figure 6.2: Mori's experimental setup [87]

Regarding these experiments, the theory behind them is more difficult to describe in simple mathematical models. This is undoubtedly due to the porous material characteristics as these make it harder to numerically predict. Even Eguchi K. et al. [88] mentioned the lack of research regarding the quantitative prediction of physics between

laser absorption, heat transfer, and radiation of porous carbon. In 2019, Mori K. et al. [89] published a paper about a simplified model for the porous heat exchanger laser rocket propulsion which involved the experimental measurement of the porous carbon's temperature distribution. This was a first-time approach which certainly requires more experimental testing to improve.

## 6.2. SOLAR THERMAL EXPERIMENTS

In the literature, there is a significant increase in the amount of experimental research regarding solar thermal propulsion compared to laser thermal propulsion. Fortunately, the indirect propulsion concept is common to both concepts and, therefore, these analyses are beneficial to laser thermal propulsion. Consequently, the most relevant studies are mentioned.

In 1997, Shimizu M. et al. [90] performed solar thermal propulsion experiments on a thruster made of single-crystal molybdenum with nitrogen as the propellant. To increase the heat transfer, spiral tubing was chosen. The temperatures of the inner cavity surface, the outer surface and the propellant fluid were measured by three platinum/rhodium thermocouples and the outer chamber was insulated with carbon felt. Additionally, a vacuum chamber was used. The test setup is displayed in fig. 6.3.

Regarding the experimental results, the temperatures were typically highest in the inner cavity surface, followed by the propellant and then the outer wall. The highest propellant temperature reached was 1850K at a 0.2 MPa chamber pressure which corresponds to 700 s of  $I_{sp}$  for hydrogen. The main problem in this setup was the solar concentrator whose faulty construction resulted in a decrease in the concentration ratio. Consequently, higher reliability and performance can be achieved by improving that component. There is no mention of overall efficiency, not even solar energy input which makes it impossible to evaluate the whole setup.

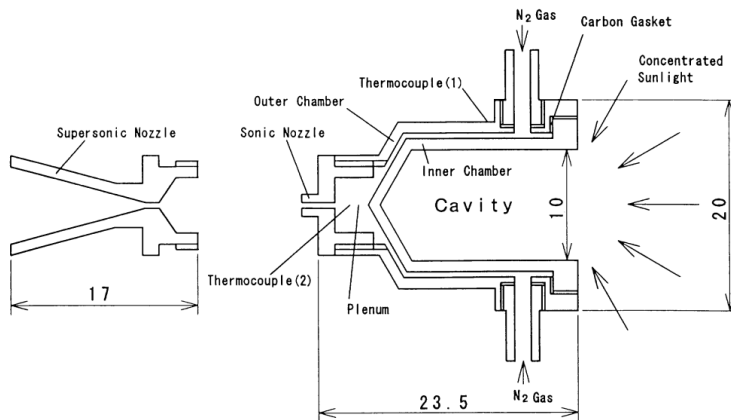


Figure 6.3: Shimizu M. et al. single crystal molybdenum solar thruster structure [90]

Tucker S. et al. [91] performed experimental testing in a rhenium engine. Unlike

the previous experiments, the heating of the inner cavity is not from a beam but rather a silicone-carbide electrical resistance heater. The tests were performed in a vacuum since rhenium oxidizes at high temperatures. Instrumentation consists of several thermocouples, pressure sensors, a flow meter, and strain gauges as shown in fig. 6.4.

The strain gauges measured the thrust due to the difference in weight when thrusting and not thrusting. Even though it was a reliable method, the outer connections such as the thermocouples and the electrical power line affected the module's centre of gravity and, consequently, the measured thrust. Thus, the thrust is higher than the measured values, approximately 20%. A maximum  $I_{sp}$  of 150 s was achieved at 960 °C which is an equivalent hydrogen  $I_{sp}$  of 630 s.

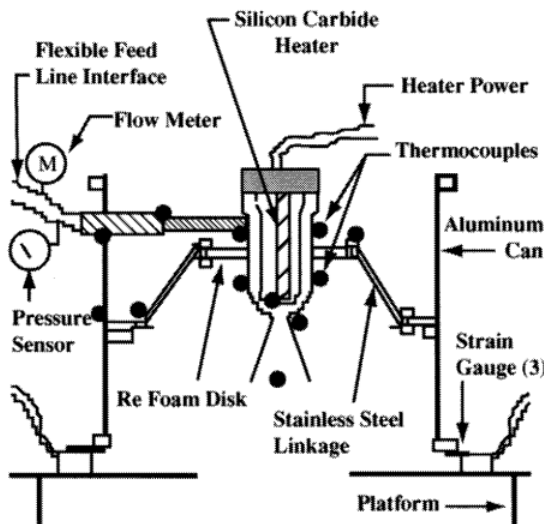


Figure 6.4: Tucker S. et al. experiment configuration [91]

In 2003, Sahara H. et al. [92] fabricated and experimented with three solar thrusters - medium, small and very small - made of single-crystal molybdenum. Again, thermocouples are used to measure the propellant and outer wall temperatures, carbon felt is used as thermal insulation and the tests are performed in a vacuum chamber. The experimental setup is very similar to the one in fig. 6.3. For the small model, the propellant reached 2300 K which corresponds to the 800 s  $I_{sp}$  hydrogen level. The medium was a 2 N-class thruster for hydrogen and nitrogen reached 1600 K. The lower temperature is a result of higher radiation losses due to increased size. Furthermore, its size required a bigger solar concentrator. The very small thruster had temperatures in between the previous two models and the performance was worse than expected because the solar image was bigger than the cavity itself and the propellant supply pipes were relatively big, resulting in huge conduction heat losses through these pipes.

### 6.3. TU DELFT EXPERIMENTS

As mentioned throughout this literature study, several students have performed work concerning solar thermal propulsion. However, regarding experimental tests, these were only performed by Leenders H. [31]. Takken A.'s main goal was also to carry out experiments but due to design changes his model was unsuitable [8]. Nevertheless, test planning was done. Since experiments are also planned to be performed, special attention is given to both students' configurations.

As the power source, Leenders H. [31] used a 1 kW incandescent theatre lamp coupled with a converging lens system to direct the beam. The propellant of choice was gaseous nitrogen. The test is performed in the Delft Aerospace Rocket Stand (DARTS) and the setup is shown in fig. 6.5. While testing, the following parameters are measured over time: thrust, chamber pressure, thruster inlet pressure, propellant temperature, RAC temperature, and mass flow rate. Concerning the experimental results, these have good agreement with the predictions and points of improvement are to increase the system's power input and optimize the RAC's design, for instance, spiral ducts. The maximum equilibrium temperature of the RAC was around 700K without mass flow and with mass flow, the equilibrium temperatures were around 525K for the RAC and 475K for the propellant. The efficiency ranged from 32% to 60%, increasing with the mass flow.

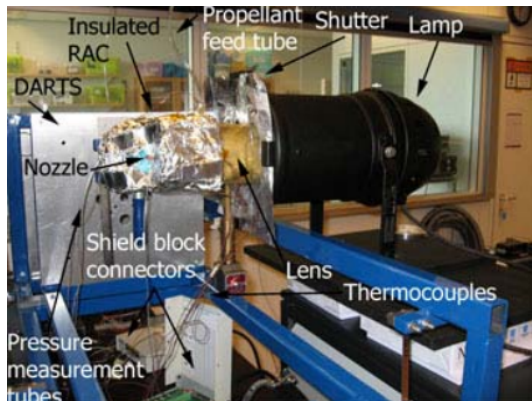


Figure 6.5: Leenders H.'s test setup [31]

Taking into account Leenders H.'s recommendations, Takken A. [8] changed the intended power source to a laser located in the welding facility of 3mE. Three different experiments were planned: test with nitrogen flow without illumination; test without nitrogen flow with illumination; and test with nitrogen flow with illumination. Thermocouples would be placed in the outer and inner surfaces of the RAC and nozzle where possible. Pressure sensors, due to their impact on the system, would be limited to two: one before the RAC and the other in the nozzle chamber. Several possible mass flow sensors available are mentioned. Regarding the thrust measurement, two thrust benches are discussed with test bench AE-TB-50m being selected due to the predicted thrust range of the experiments. Takken A. had to rebuild the test bench and his steps are fairly documented in his thesis. The problems with the model were related to the extremely

high-pressure loss in the RAC and the existence of leaks. Thus, special attention needs to be given when making design changes as well as excluding thread connections and allowing hard-soldered connections.

# 7

## CONCLUSION

Current spacecraft propulsion systems entail limitations that present themselves as an obstacle regarding increased interplanetary exploration and missions. The laser thermal propulsion concept is one of the proposed alternatives to surpass these obstacles due to its capacity to achieve high specific impulses with not-so-small thrusts. In this literature study, the several components of a laser thermal propulsion system, the crucial physics inherent to them and relevant experimental setups were researched.

Firstly, the laser system was investigated. Relevant laser physics such as beam attenuation and divergence were explored. Additionally, a concise trade-off between the location of the laser system was conducted. Although, an earth-based laser is the most attainable, a laser spacecraft might be the actual answer for the success of laser thermal propulsion. Next, a few outlines of the reflective/optical system were done, mainly its capacity to achieve high efficiencies as well as its temperature constraints and weight.

The RAC was the main focus of the research. Initially, its possible configuration and efficiencies were defined. From a geometrical point of view, the conical shape appears to have benefits regarding the cylindrical one. However, most of the evidence supporting such is not fully appropriate to laser thermal propulsion since, for instance, the aperture ratio was unitary and the beam was not constant. Consequently, three final shapes were deemed relevant to study further: conical, cylindrical and conical with a cylindrical bottom. Furthermore, the RAC material options from the literature were discussed. The relevance of radiation, convection and conduction was examined. The main absence of information in the literature is related to the fraction of laser energy absorbed in a cavity. This is a fundamental concern that requires investigation. Pressure gradients were also presented. Finally, a RAC tool created with Matlab was introduced, verified and validated.

After, the nozzle subsystem was introduced as well as the ideal rocket theory fundamentals. The common nozzle geometries were mentioned and commented on. Moreover, correction factors to approximate the ideal estimates to real performance were introduced and their relation was discussed. Finally, a nozzle tool was also created and validated with previous student work.

Concerning the propellant system, initially, the most common storage and feeding systems in space propulsion were mentioned. More importantly, the propellant choices found in the literature were presented as well as the comments made by each researcher about their findings. Although hydrogen is the most promising propellant, it does not offer enough safety to be used in a thesis experiment. Consequently, water, nitrogen and helium are the main candidates for such activities.

Despite extensive investigation, a significant amount of experimental research regarding laser thermal propulsion concerning indirect heating was not found. In fact, only two experiments using porous carbon as the heat exchanger were found. The main losses in these experiments were due to the emitted radiation. Nevertheless, their experimental setups are extremely useful. To cover this lack of experiments, solar thermal experiments were also discussed since their setups are pretty similar. Again, their results and experimental setups are undeniably valuable for an experimental thesis.

To sum up, throughout this literature study, extensive research has been conducted regarding laser thermal propulsion systems and their components. A fundamental understanding of the physics, current state-of-the-art and experimental research concerning laser thermal propulsion was gained. Consequently, the author is irrefutably prepared to pursue a relevant thesis in the area.

# BIBLIOGRAPHY

- [1] McGill University. *Spacecraft propulsion*. 2007. URL: [https://www.cs.mcgill.ca/~rwest/wikispeedia/wpcd/wp/s/Spacecraft\\_propulsion.htm](https://www.cs.mcgill.ca/~rwest/wikispeedia/wpcd/wp/s/Spacecraft_propulsion.htm) (visited on 11/19/2022).
- [2] Eun S. Kim, Jeffery L. Emdee, and Richard K. Cohn. “Liquid Propulsion: Historical Overview, Fundamentals, and Classifications of Liquid Rocket Engines”. In: *Encyclopedia of Aerospace Engineering*. John Wiley Sons, Ltd, 2010. ISBN: 9780470686652.
- [3] Shashi Kant Shrivastava. “Orbital perturbations and stationkeeping of communication satellites”. In: *Journal of Spacecraft and Rockets* 15.2 (1978), pp. 67–78.
- [4] B.T.C. Zandbergen. *AE4-S01 Thermal Rocket Propulsion (version 2.08)*. Aug. 2020.
- [5] Harold P. Gerrish Jr. *Solar Thermal Propulsion at MSFC*. Propulsion Systems Division Marshall Space Flight Center. Feb. 2016. URL: <https://ntrs.nasa.gov/api/citations/20160003173/downloads/20160003173.pdf> (visited on 11/2022).
- [6] Emmanuel Duplay et al. “Design of a rapid transit to Mars mission using laser-thermal propulsion”. In: *Acta Astronautica* 192 (2022), pp. 143–156. ISSN: 0094-5765. DOI: <https://doi.org/10.1016/j.actaastro.2021.11.032>. URL: <https://www.sciencedirect.com/science/article/pii/S0094576521006305>.
- [7] Fiona Leverone et al. “Design and characterisation of a bi-modal solar thermal propulsion and power system for small satellites”. In: *Applied Thermal Engineering* 189 (2021), p. 116609. ISSN: 1359-4311. DOI: <https://doi.org/10.1016/j.applthermaleng.2021.116609>. URL: <https://www.sciencedirect.com/science/article/pii/S135943112100065X>.
- [8] A. Takken. *Development of a high temperature Solar Thermal Propulsion engine*. 2021.
- [9] Roland Antonius Gabrielli and Georg Herdrich. “Review of nuclear thermal propulsion systems”. In: *Progress in Aerospace Sciences* 79 (2015), pp. 92–113.
- [10] R. A. Ferreira. *Development and testing of a water resistojet*. 2008.
- [11] Birk Wollenhaupt, Quang Hoa Le, and Georg Herdrich. “Overview of thermal arcjet thruster development”. In: *Aircraft Engineering and Aerospace Technology* (2018).
- [12] Anthony E Siegman. *Lasers*. University science books, 1986.
- [13] Marc Sulfridge et al. “Optical actuation of a bistable MEMS”. In: *Microelectromechanical Systems, Journal of* 11 (Nov. 2002). DOI: [10.1109/JMEMS.2002.803417](https://doi.org/10.1109/JMEMS.2002.803417).
- [14] V. Shcherbakov et al. “Multi-Kilowatt CW Fiber Laser Systems with Record Wall-Plug Efficiency Exceeding 50%”. In: June 2016.

- [15] DG Lancaster et al. "Fifty percent internal slope efficiency femtosecond direct-written Tm 3+: ZBLAN waveguide laser". In: *Optics Letters* 36.9 (2011), pp. 1587–1589.
- [16] RJ Deyoung et al. *Preliminary design and cost of a 1-megawatt solar-pumped iodide laser space-to-space transmission station*. Tech. rep. 1987.
- [17] Rémi Soulard et al. "ICAN: A novel laser architecture for space debris removal". In: *Acta Astronautica* 105.1 (2014), pp. 192–200. ISSN: 0094-5765. DOI: <https://doi.org/10.1016/j.actaastro.2014.09.004>. URL: <https://www.sciencedirect.com/science/article/pii/S0094576514003397>.
- [18] Thomas Fahey et al. "Laser Beam Atmospheric Propagation Modelling for Aerospace LIDAR Applications". In: *Atmosphere* 12.7 (2021). ISSN: 2073-4433. URL: <https://www.mdpi.com/2073-4433/12/7/918>.
- [19] Will Hettel et al. "Beam propagation simulation of phased laser arrays with atmospheric perturbations". In: *Appl. Opt.* 60.17 (June 2021), pp. 5117–5123. DOI: <10.1364/AO.422337>. URL: <https://opg.optica.org/ao/abstract.cfm?URI=ao-60-17-5117>.
- [20] Isaac Kim, Bruce Mcarthur, and Eric Korevaar. "Comparison of laser beam propagation at 785 nm and 1550 nm in fog and haze for optical wireless communications". In: *Proc. SPIE* 4214 (Feb. 2001). DOI: <10.1117/12.417512>.
- [21] H. Weichel. *Laser Beam Propagation in the Atmosphere*. Proceedings of SPIE—the International Society for Optical Engineering. SPIE Optical Engineering Press, 1990. ISBN: 9780819404879. URL: <https://books.google.nl/books?id=0zkZ0o5SRj8C>.
- [22] John W. Pepi and Richard J. Wollensak. "Ultra-Lightweight Fused Silica Mirrors For A Cryogenic Space Optical System". In: *Space Optics II*. Ed. by Charles L. Wyman. Vol. 0183. International Society for Optics and Photonics. SPIE, 1979, pp. 131–137. DOI: <10.1117/12.957406>. URL: <https://doi.org/10.1117/12.957406>.
- [23] M Salama, M Lou, and H Fang. "Deployment of inflatable space structures—a review of recent developments". In: *41st Structures, Structural Dynamics, and Materials Conference and Exhibit*. 2000, p. 1730.
- [24] D. Pino. *Solar Concentrator Demonstrator for PocketQubes*. 2016.
- [25] Steve E. Watkins, J. Paul Black, and Bradley J. Pond. "Optical scatter characteristics of high-reflectance dielectric coatings and fused-silica substrates". In: *Appl. Opt.* 32.28 (Oct. 1993), pp. 5511–5518. DOI: <10.1364/AO.32.005511>. URL: <https://opg.optica.org/ao/abstract.cfm?URI=ao-32-28-5511>.
- [26] F.M. Dickey. *Laser Beam Shaping: Theory and Techniques, Second Edition*. CRC Press, 2018. ISBN: 9781466561014. URL: [https://books.google.nl/books?id=Ph%5C\\_cBQAAQBAJ](https://books.google.nl/books?id=Ph%5C_cBQAAQBAJ).
- [27] Yagiz Kaymak et al. "A Survey on Acquisition, Tracking, and Pointing Mechanisms for Mobile Free-Space Optical Communications". In: *IEEE Communications Surveys Tutorials* 20.2 (2018), pp. 1104–1123. DOI: <10.1109/COMST.2018.2804323>.

- [28] Xiaoning Jiang, William B. Cook, and Wesley S. Hackenberger. "Cryogenic piezo-electric actuators". In: *Astronomical and Space Optical Systems*. Ed. by Penny G. Warren et al. Vol. 7439. International Society for Optics and Photonics. SPIE, 2009, 74390Z. DOI: [10.1117/12.826341](https://doi.org/10.1117/12.826341). URL: <https://doi.org/10.1117/12.826341>.
- [29] K. Das. *Design and Thermal Analysis of a Solar Thermal Thruster*. 2018.
- [30] A. Takken. *Feasibility of Solar Thermal Propulsion Literature Study*. 2019.
- [31] HCM Leenders and BTC Zandbergen. "Development of a solar thermal thruster system". In: *59th International Astronautical Congress: IAC 2008, 29 September-3 October 2008, Glasgow, Scotland*. 2008.
- [32] J. SHOJI and V. LARSON. "Performance and heat transfer characteristics of the laser-heated rocket - A future space transportation system". In: *12th International Electric Propulsion Conference*. DOI: [10.2514/6.1976-1044](https://arc.aiaa.org/doi/pdf/10.2514/6.1976-1044). eprint: <https://arc.aiaa.org/doi/pdf/10.2514/6.1976-1044>. URL: <https://arc.aiaa.org/abs/10.2514/6.1976-1044>.
- [33] Ahmed M. Daabo, Saad Mahmoud, and Raya K. Al-Dadah. "The effect of receiver geometry on the optical performance of a small-scale solar cavity receiver for parabolic dish applications". In: *Energy* 114 (2016), pp. 513–525. ISSN: 0360-5442. DOI: <https://doi.org/10.1016/j.energy.2016.08.025>. URL: <https://www.sciencedirect.com/science/article/pii/S0360544216311288>.
- [34] J. H. Lienhard IV and J. H. Lienhard V. *A Heat Transfer Textbook*. 5th. Version 5.10. Cambridge, MA: Phlogiston Press, 2020. URL: <http://ahtt.mit.edu>.
- [35] Tom van Boxtel. *AE4S20 Satellite Thermal Control Lecture Notes*. 2021.
- [36] JM Shoji. *Solar rocket component study*. Tech. rep. ROCKWELL INTERNATIONAL CANOGA PARK CA ROCKETDYNE DIV, 1985.
- [37] C.-A. Asselineau, J. Zapata, and J. Pye. "Geometrical Shape Optimization of a Cavity Receiver Using Coupled Radiative and Hydrodynamic Modeling". In: *Energy Procedia* 69 (2015). International Conference on Concentrating Solar Power and Chemical Energy Systems, SolarPACES 2014, pp. 279–288. ISSN: 1876-6102. DOI: <https://doi.org/10.1016/j.egypro.2015.03.032>. URL: <https://www.sciencedirect.com/science/article/pii/S1876610215003380>.
- [38] B. Gebhart. *Heat Transfer*. McGraw-Hill, 1961.
- [39] J. J. Preijde. *Design of a Solar Thermal Power-Propulsion System for a Small Satellite*. 2015.
- [40] Engineering Toolbox. *The Engineering Toolbox Data Base*. Accessed: 2023-01-29. 2023. URL: <https://www.engineeringtoolbox.com/>.
- [41] Leonland. *Chemical elements by market price*. Accessed: 2023-01-30. 2023. URL: [http://www.leonland.de/elements\\_by\\_price/en/list](http://www.leonland.de/elements_by_price/en/list).
- [42] Jordin Kare. "High Performance Heat Exchanger for Laser Propulsion". In: *36th AIAA Plasmadynamics and Lasers Conference*. DOI: [10.2514/6.2005-5176](https://arc.aiaa.org/doi/pdf/10.2514/6.2005-5176). eprint: <https://arc.aiaa.org/doi/pdf/10.2514/6.2005-5176>. URL: <https://arc.aiaa.org/abs/10.2514/6.2005-5176>.

- [43] F. G. Kennedy and Palmer P.L. "Preliminary Design of a Micro-scale Solar Thermal Propulsion System". In: *38th AIAA/ASME/SAE/ASEE Joint Propulsion Conference & Exhibit*. 2002. DOI: [10.2514/6.2002-3928](https://doi.org/10.2514/6.2002-3928). URL: <https://arc.aiaa.org/doi/abs/10.2514/6.2002-3928>.
- [44] Kurt O. Westerman and Barry J. Miles. "Testing of a Receiver-Absorber-Converter (RAC) for the Integrated Solar Upper Stage (ISUS) program". In: *AIP Conference Proceedings* 420.1 (1998), pp. 375–380. DOI: [10.1063/1.54822](https://doi.org/10.1063/1.54822). eprint: <https://aip.scitation.org/doi/pdf/10.1063/1.54822>. URL: <https://aip.scitation.org/doi/abs/10.1063/1.54822>.
- [45] J. SHOJI. "Performance potential of advanced solar thermal propulsion". In: *19th Joint Propulsion Conference*. DOI: [10.2514/6.1983-1307](https://doi.org/10.2514/6.1983-1307). eprint: <https://arc.aiaa.org/doi/pdf/10.2514/6.1983-1307>. URL: <https://arc.aiaa.org/doi/abs/10.2514/6.1983-1307>.
- [46] Keisuke Eguchi et al. "Fundamental Experiment of CW Laser Propulsion with Porous Carbon Heat Exchanger". In: *2018 AIAA Aerospace Sciences Meeting*. DOI: [10.2514/6.2018-0176](https://doi.org/10.2514/6.2018-0176). eprint: <https://arc.aiaa.org/doi/pdf/10.2514/6.2018-0176>. URL: <https://arc.aiaa.org/doi/abs/10.2514/6.2018-0176>.
- [47] Koichi Mori. "Laser Propulsion Using a Porous Carbon Heat Exchanger". In: *Journal of Propulsion and Power* 38.5 (2022), pp. 880–883. DOI: [10.2514/1.B38613](https://doi.org/10.2514/1.B38613). eprint: <https://doi.org/10.2514/1.B38613>. URL: <https://doi.org/10.2514/1.B38613>.
- [48] Florent Larrouturou, Cyril Caliot, and Gilles Flamant. "Effect of directional dependency of wall reflectivity and incident concentrated solar flux on the efficiency of a cavity solar receiver". In: *Solar Energy* 109 (2014), pp. 153–164. ISSN: 0038-092X. DOI: <https://doi.org/10.1016/j.solener.2014.08.028>. URL: <https://www.sciencedirect.com/science/article/pii/S0038092X14004058>.
- [49] P M Sutheesh and Alex Chollackal. "Thermal performance of multilayer insulation: A review". In: *IOP Conference Series: Materials Science and Engineering* 396.1 (Aug. 2018), p. 012061. DOI: [10.1088/1757-899X/396/1/012061](https://doi.org/10.1088/1757-899X/396/1/012061). URL: <https://dx.doi.org/10.1088/1757-899X/396/1/012061>.
- [50] SAFFIL M-FIL PRODUCT DATA SHEET. SAFFIL. URL: <http://www.lloyd-ris.co.uk/pdfs/datasheets/SAFFIL%20M%20FIL%20DATA%20Sheet.pdf>.
- [51] European Space Agency. "Spacecraft thermal-control design data handbook – Volume 1". In: European Space Agency, 1989.
- [52] J. H. Chin, T. D. Panczak, and L. Fried. "Spacecraft thermal modelling". In: *International Journal for Numerical Methods in Engineering* 35.4 (1992), pp. 641–653. DOI: <https://doi.org/10.1002/nme.1620350403>. eprint: <https://onlinelibrary.wiley.com/doi/pdf/10.1002/nme.1620350403>. URL: <https://onlinelibrary.wiley.com/doi/abs/10.1002/nme.1620350403>.
- [53] Ravindra Jilte, S.B. Kedare, and J.K. Nayak. "Natural Convection and Radiation Heat Loss from Open Cavities of Different Shapes and Sizes Used with Dish Concentrator". In: *Mechanical Engineering Research* 3 (Jan. 2013). DOI: [10.5539/mer.v3n1p25](https://doi.org/10.5539/mer.v3n1p25).

- [54] Subhashis Ray, Alexandra Loukou, and Dimosthenis Trimis. "Evaluation of heat conduction through truncated conical shells". In: *International Journal of Thermal Sciences* 57 (2012), pp. 183–191. ISSN: 1290-0729. DOI: <https://doi.org/10.1016/j.ijthermalsci.2012.02.004>. URL: <https://www.sciencedirect.com/science/article/pii/S129007291200049X>.
- [55] Edward L Wilson and Robert E Nickell. "Application of the finite element method to heat conduction analysis". In: *Nuclear engineering and design* 4.3 (1966), pp. 276–286.
- [56] W.M. Rohsenow, J.P. Hartnett, and Y.I. Cho. *Handbook of Heat Transfer*. McGraw-Hill handbooks. McGraw-Hill Education, 1998. ISBN: 9780070535558.
- [57] M. Prakash, S.B. Kedare, and J.K. Nayak. "Investigations on heat losses from a solar cavity receiver". In: *Solar Energy* 83.2 (2009), pp. 157–170. ISSN: 0038-092X. DOI: <https://doi.org/10.1016/j.solener.2008.07.011>. URL: <https://www.sciencedirect.com/science/article/pii/S0038092X08001795>.
- [58] R. Uhlig et al. "Strategies Enhancing Efficiency of Cavity Receivers". In: *Energy Procedia* 49 (2014). Proceedings of the SolarPACES 2013 International Conference, pp. 538–550. ISSN: 1876-6102. DOI: <https://doi.org/10.1016/j.egypro.2014.03.058>. URL: <https://www.sciencedirect.com/science/article/pii/S1876610214005128>.
- [59] M. Prakash, S.B. Kedare, and J.K. Nayak. "Numerical study of natural convection loss from open cavities". In: *International Journal of Thermal Sciences* 51 (2012), pp. 23–30. ISSN: 1290-0729. DOI: <https://doi.org/10.1016/j.ijthermalsci.2011.08.012>. URL: <https://www.sciencedirect.com/science/article/pii/S129007291100250X>.
- [60] S. Paitoonsurikarn et al. "Numerical Investigation of Natural Convection Loss From Cavity Receivers in Solar Dish Applications". In: *Journal of Solar Energy Engineering* 133.2 (Mar. 2011). 021004. ISSN: 0199-6231. DOI: [10.1115/1.4003582](https://doi.org/10.1115/1.4003582). eprint: [https://asmedigitalcollection.asme.org/solarenergyengineering/article-pdf/133/2/021004/5714926/021004\\_1.pdf](https://asmedigitalcollection.asme.org/solarenergyengineering/article-pdf/133/2/021004/5714926/021004_1.pdf). URL: <https://doi.org/10.1115/1.4003582>.
- [61] Ke Wang et al. "A numerical study on the natural convective heat loss of an isothermal upward-facing cylindrical cavity". In: *Applied Thermal Engineering* 213 (2022), p. 118763. ISSN: 1359-4311. DOI: <https://doi.org/10.1016/j.applthermaleng.2022.118763>. URL: <https://www.sciencedirect.com/science/article/pii/S1359431122007050>.
- [62] Sawat Paitoonsurikarn and Keith Lovegrove. "On the Study of Convection Loss from Open Cavity Receivers in Solar Paraboloidal Dish Applications". In: *Proceedings of 41st Conference of the Australia and New Zealand Solar Energy Society (ANZSES)* (Jan. 2004).
- [63] T.L. Bergman et al. *Fundamentals of Heat and Mass Transfer*. Wiley, 2011. ISBN: 9780470501979. URL: <https://books.google.nl/books?id=vvyIoXEywMoC>.
- [64] S Kakac, R K Shah, and W Aung. "Handbook of single-phase convective heat transfer". In: (Jan. 1987). URL: <https://www.osti.gov/biblio/6291382>.

- [65] S.E. Haaland. *Simple and Explicit Formulas for the Friction Factor in Turbulent Pipe Flow, Including Natural Gas Pipelines*. Univ., Norwegian Inst. of Technol., Division of Aero- and Gas Dynamics, 1981. URL: <https://books.google.nl/books?id=veHGPgAACAAJ>.
- [66] V. Gnielinski. "New equations for heat and mass transfer in the turbulent flow in pipes and channels". In: *NASA STI/Recon Technical Report A41.1* (Jan. 1975), pp. 8–16.
- [67] Taler, Dawid and Taler, Jan. "Simple heat transfer correlations for turbulent tube flow". In: *E3S Web Conf. 13* (2017), p. 02008. DOI: [10.1051/e3sconf/20171302008](https://doi.org/10.1051/e3sconf/20171302008). URL: <https://doi.org/10.1051/e3sconf/20171302008>.
- [68] Nikolay Kolev. "Multiphase Flow Dynamics 3". In: Jan. 2011, pp. 35–66. ISBN: 978-3-642-21371-7. DOI: [10.1007/978-3-642-21372-4\\_2](https://doi.org/10.1007/978-3-642-21372-4_2).
- [69] M. Massoud. *Engineering Thermofluids: Thermodynamics, Fluid Mechanics, and Heat Transfer*. Springer Berlin Heidelberg, 2005. ISBN: 9783540272809. URL: [https://books.google.nl/books?id=9KIp%5C\\_fmC9AOC](https://books.google.nl/books?id=9KIp%5C_fmC9AOC).
- [70] P. Oosthuizen. "Free Convective Heat Transfer From Horizontal Cones". In: *ASME* (1973).
- [71] P. H. Oosthuizen and E. Donaldson. "Free Convective Heat Transfer from Vertical Cones". In: *Journal of Heat Transfer* 94.3 (Aug. 1972), pp. 330–331. ISSN: 0022-1481. DOI: [10.1115/1.3449945](https://doi.org/10.1115/1.3449945). eprint: [https://asmedigitalcollection.asme.org/heattransfer/article-pdf/94/3/330/5728271/330\\\_1.pdf](https://asmedigitalcollection.asme.org/heattransfer/article-pdf/94/3/330/5728271/330\_1.pdf). URL: <https://doi.org/10.1115/1.3449945>.
- [72] Stuart W. Churchill and Humbert H.S. Chu. "Correlating equations for laminar and turbulent free convection from a horizontal cylinder". In: *International Journal of Heat and Mass Transfer* 18.9 (1975), pp. 1049–1053. ISSN: 0017-9310. DOI: [https://doi.org/10.1016/0017-9310\(75\)90222-7](https://doi.org/10.1016/0017-9310(75)90222-7). URL: <https://www.sciencedirect.com/science/article/pii/0017931075902227>.
- [73] Jerod Day, Matthew Traum, and Sandra Boetcher. "Laminar Natural Convection From Isothermal Vertical Cylinders: A Revisit to a Classical Subject". In: vol. 135. Mar. 2011. DOI: [10.1115/AJTEC2011-44552](https://doi.org/10.1115/AJTEC2011-44552).
- [74] Liejin Guo, Ziping Feng, and Xuejun Chen. "An experimental investigation of the frictional pressure drop of steam–water two-phase flow in helical coils". In: *International Journal of Heat and Mass Transfer* 44.14 (2001), pp. 2601–2610. ISSN: 0017-9310. DOI: [https://doi.org/10.1016/S0017-9310\(00\)00312-4](https://doi.org/10.1016/S0017-9310(00)00312-4). URL: <https://www.sciencedirect.com/science/article/pii/S0017931000003124>.
- [75] D. Chisholm. "A theoretical basis for the Lockhart-Martinelli correlation for two-phase flow". In: *International Journal of Heat and Mass Transfer* 10.12 (1967), pp. 1767–1778. ISSN: 0017-9310. DOI: [https://doi.org/10.1016/0017-9310\(67\)90047-6](https://doi.org/10.1016/0017-9310(67)90047-6). URL: <https://www.sciencedirect.com/science/article/pii/0017931067900476>.

- [76] Marine Narcy and Catherine Colin. "Two-phase pipe flow in microgravity with and without phase change: recent progress and future prospects". In: *Interfacial Phenomena and Heat Transfer* 3.1 (2015).
- [77] Wilfried Roetzel, Xing Luo, and Dezhen Chen. "Chapter 2 - Basic thermal design theory for heat exchangers". In: *Design and Operation of Heat Exchangers and their Networks*. Ed. by Wilfried Roetzel, Xing Luo, and Dezhen Chen. Academic Press, 2020, pp. 13–69. ISBN: 978-0-12-817894-2. DOI: <https://doi.org/10.1016/B978-0-12-817894-2.00002-9>. URL: <https://www.sciencedirect.com/science/article/pii/B9780128178942000029>.
- [78] *The Barlow Equation for Tubular Burst: A Muddled History*. Vol. Day 3 Thu, March 08, 2018. SPE/IADC Drilling Conference and Exhibition. D031S013R001. Mar. 2018. DOI: [10.2118/189681-MS](https://doi.org/10.2118/189681-MS). eprint: <https://onepetro.org/SPEDC/proceedings-pdf/18DC/3-18DC/D031S013R001/1227587/spe-189681-ms.pdf>. URL: <https://doi.org/10.2118/189681-MS>.
- [79] Dipesh D Shukla, Niraj C Mehta, and Ravi K Popat. "Optimisation of Wall Thickness for Minimum Heat Loss for Induction Furnace by FEA". In: *Indian Foundry Journal* 60.12 (2014).
- [80] Z Li, SC Mantell, and JH Davidson. "Mechanical analysis of streamlined tubes with non-uniform wall thickness for heat exchangers". In: *The Journal of Strain Analysis for Engineering Design* 40.3 (2005), pp. 275–285.
- [81] George P Sutton and Oscar Biblarz. *Rocket propulsion elements*. John Wiley & Sons, 2016.
- [82] Aaron N Johnson et al. "Numerical characterization of the discharge coefficient in critical nozzles". In: *NCSL Conference Proceedings, Albuquerque, NM*. 1998, pp. 407–422.
- [83] Jeff Berton. "Divergence Thrust Loss Calculations for Convergent-Divergent Nozzles: Extensions to the Classical Case". In: (Jan. 1991). DOI: [10.13140/RG.2.1.4257.5446](https://doi.org/10.13140/RG.2.1.4257.5446).
- [84] C. Mayes et al. *Boundary-Layer Theory*. Physic and astronomy. Springer Berlin Heidelberg, 2003. ISBN: 9783540662709. URL: <https://books.google.nl/books?id=8YugVtom1y4C>.
- [85] Hendrik Tennekes, John Leask Lumley, Jonh L Lumley, et al. *A first course in turbulence*. MIT press, 1972.
- [86] Wilfried Ley, Klaus Wittmann, and Willi Hallmann. *Handbook of space technology*. John Wiley & Sons, 2009.
- [87] Koichi Mori. "Laser Propulsion Using a Porous Carbon Heat Exchanger". In: *Journal of Propulsion and Power* 38.5 (2022), pp. 880–883.
- [88] Keisuke Eguchi et al. "Fundamental Experiment of CW Laser Propulsion with Porous Carbon Heat Exchanger". In: *2018 AIAA Aerospace Sciences Meeting*. 2018, p. 0176.

- [89] Koichi Mori and Hiroki Itoh. "A Simplified Model for The Thrust Performance of Porous Heat eXchanger (PHX) Laser Rocket Propulsion". In: *AIAA Propulsion and Energy 2019 Forum*. DOI: [10.2514/6.2019-3802](https://doi.org/10.2514/6.2019-3802). eprint: <https://arc.aiaa.org/doi/pdf/10.2514/6.2019-3802>. URL: <https://arc.aiaa.org/doi/abs/10.2514/6.2019-3802>.
- [90] Morio Shimizu et al. "Solar thermal thruster made of single crystal molybdenum Paper IAF-96-S.4.01, presented at the 47th International Astronautical Congress, Beijing, China, 7–11 October 1996." In: *Acta Astronautica* 41.1 (1997), pp. 23–28. ISSN: 0094-5765. DOI: [https://doi.org/10.1016/S0094-5765\(97\)00200-2](https://doi.org/10.1016/S0094-5765(97)00200-2). URL: <https://www.sciencedirect.com/science/article/pii/S0094576597002002>.
- [91] Stephen Tucker and Pat Salvail. "Solar-thermal engine testing". In: *AIP Conference Proceedings*. Vol. 608. 1. American Institute of Physics. 2002, pp. 486–493.
- [92] Hironori Sahara et al. "Single-crystal molybdenum solar thermal propulsion thruster". In: *Transactions of the Japan Society for Aeronautical and Space Sciences* 46.153 (2003), pp. 180–185.